Bearing capacity and failure mechanism of strip footings on anisotropic sand

Zhiwei Gao[1*], Dechun Lu[2], Xiuli Du[3]

[1] Lecturer, James Watt School of Engineering, University of Glasgow, Glasgow, G12 8QQ, UK

[2] Professor, Key Laboratory of Urban Security and Disaster Engineering of Ministry of Education, Beijing University of Technology, Beijing 100124, China

[3] Professor, Key Laboratory of Urban Security and Disaster Engineering of Ministry of Education, Beijing University of Technology, Beijing 100124, China

[*]Corresponding author: Email: zhiwei.gao@glasgow.ac.uk; Tel: +44 1413303927

Abstract: Sand typically exhibits anisotropic internal structure (or fabric) and the fabric anisotropy has dramatic influence on mechanical behaviour of sand. Meanwhile, the fabric evolves when sand is subjected to external loading. This eventually makes the response of strip footings on sand dependent on fabric anisotropy and fabric evolution. A numerical investigation on this effect is presented using a critical state sand model accounting for fabric evolution. The model parameters are determined based on plane strain and triaxial compression test data and the model performance is validated by centrifuge tests for strip footings on dry Toyoura sand. The bearing capacity of strip footings is found to be dependent on bedding plane orientation of dense sand. But this effect vanishes as the sand density decreases, though the slope of the force-displacement curve is still lower for horizontal bedding. Progressive failure is observed for all the simulations. General shear failure mode occurs in dense and medium dense sand and punching shear mode is the main failure mechanism for loose sand. In general shear failure, unsymmetrical slip lines develop for sand with inclined bedding plane due to the noncoaxial sand behaviour caused by fabric anisotropy. For strip footing on sand with horizontal bedding, the bearing capacity and failure mechanism is primarily affected by the sand density. The bearing capacity of a strip footing is higher when the sand fabric is more isotropic for the same soil density. An isotropic model can give significant overestimation on the bearing capacity of strip footings.

Keywords: Anisotropy; fabric evolution; sand; bearing capacity; strip footing

Introduction

It is well recognized that both man-made and natural sand deposits always have anisotropic internal structure (or fabric) due to compaction and gravitational loading. The fabric anisotropy can be caused by preferred orientation of particles, contact force directions or void spaces etc. The mechanical behaviour of sand, such as shear strength and volume change, is significantly affected by the fabric anisotropy (Muir and Toki, 1982; Oda and Kazama, 1998; Wan and Guo, 2001). An important feature of sand fabric is that it evolves with deformation, which in turn affects the soil behaviour (Li and Li, 2009; Fu and Dafalias, 2011; Li and Dafalias, 2012; Guo and Zhao, 2013). There has been extensive research on the anisotropic stress-strain relationship of sand using either laboratory tests or micromechanical studies (e.g., Oda et al., 1978; Azami et al., 2010; Thornton and Zhang, 2010; Guo and Zhao, 2016; Chang and Yin, 2009; Yin et al., 2010; Yin et al., 2014; Zhao et al., 2018), based on which some constitutive models have been proposed (e.g., Nemat-Nasser and Zhang, 2002; Li and Dafalias, 2012; Gao et al., 2014; Papadimitriou et al., 2019).

The fabric anisotropy and fabric evolution has influence on not only the mechanical behaviour of sand elements but also the response of infrastructure built on or using sand, such as foundations, slopes, suction caissons and offshore embedded anchors. Particularly, there has been huge interest on the bearing capacity Q_u of shallow foundations on sand, which is a classical problem in soil mechanics. Several small-scale 1g tests have been reported on sand with different bedding plane orientation, which is typically described by an angle (α) between the horizontal direction and plane of sand deposition (Oda et al., 1978; Oda and Koishikawa, 1979; Azami et al., 2010; Kawamura and Muira, 2014). It is found that Q_u of a strip footing on dense sand is the highest and lowest when bedding plane is horizontal and vertical, respectively. This difference can reach up to 25% for very dense sand. But such difference in Q_u caused by α vanishes when the relative density of sand D_r is below 70% (Oda et al., 1978; Oda and Koishikawa, 1979). Similar observations have been reported in centrifuge tests on dry Toyoura sand (Kimura et al., 1985). For strip footings on sand with horizontal bedding, which is of importance for practical applications, the fabric anisotropy must be properly considered in calculating the Q_u as well. It is shown that, without proper consideration of the strength anisotropy of sand, one may overestimate the bearing capacity factor for a shallow foundation by as much as eight times when using the classical bearing capacity theory (Guo, 2008). Chaloulos et al. (2019) have shown that Q_u of a strip footing can be overestimated by 30% using an isotropic critical sand model where the fabric effect on mechanical behaviour of sand is neglected.

Indeed, many attempts have been made in determining or modelling the Q_u of shallow foundations on sand with consideration of anisotropy. Meyerhof (1978) was the first to propose a method for calculating the Q_u of strip footings on anisotropic cohesionless soil using the plastic equilibrium approach. It is assumed that the peak friction angle is a function of α, which means that the effect of α on Q_u is independent of soil density. This method has two major limitations. First, it works for dense sand but not loose sand, because the effect of α on Q_u vanishes when D_r is low, although the peak friction angle is always dependent on α, irrespective of the soil density. Secondly, the expression for friction angle variation with loading direction is only valid for sand with horizontal bedding plane, which limits the application of this method for more general cases (Azami et al., 2010). Siddiquee et al. (1999) used finite element modelling to investigate the response of strip footings on anisotropic sand. Though the effect of α on Q_u can be reproduced, an approach similar to that in Meyerhof (1978) was used to describe the strength anisotropy of sand. Azami et al. (2010) carried out a series of small-scale 1g model tests of strip footings on sand with different α and used finite element modelling to analyse the results using a new constitutive model. Satisfactory agreement between the numerical results and test data was achieved. But this model cannot account for the effect of sand density on the soil response. Yuan et al. (2018) used pure numerical modelling to show that the strength anisotropy and non-coaxial sand behaviour should be accounted for in calculating the Q_u and settlement of strip footings. Chaloulos et al. (2019) reported comprehensive study on the response of strip footings on anisotropic sand using a newly developed sand model based on the anisotropic critical state theory (Papadimitriou et al., 2019). It is shown that the model is capable of capturing the effect of both anisotropy and density on the strip footing response. As the model employs a coaxial flow rule, it is not able to predict the formation of unsymmetrical slip lines in sand caused by inclined bedding plane orientation, which has been observed in many model tests (Azami et al., 2010; Kawamura and Muira, 2014).

This paper presents new finite element study on the response of strip footings on anisotropic sand. A critical state sand model accounting for fabric evolution is used. An important feature of the model is that it employs a non-coaxial flow rule which is dependent the current stress and fabric state. This allows the model to predict unsymmetrical slip lines under strip footing on sand with inclined bedding plane orientation ($\alpha \neq 0°$ and $\alpha \neq 90°$). The model performance will be validated against both element tests and centrifuge tests on Toyoura sand. The numerical simulations will look into the effect of α, density and initial degree of anisotropy F_0 on the Q_u and failure mechanism of strip footings. Prediction of an isotropic model for the centrifuge tests will be shown to demonstrate the importance of considering fabric anisotropy in modelling the strip footing response. Practical implications of the numerical results will be discussed. The model will first be introduced in the following, based on which the numerical implementation and finite element simulations will be presented.

A Constitutive Model for Sand Accounting for Fabric Evolution

Model formulation

The model used in this study is based on the one in Gao et al. (2014). It employs a fabric tensor for quantifying the anisotropic internal structure of sand. Fabric evolution and its effect on sand response is considered. Some minor changes have been made in the original model for the sake of numerical implementation. Specifically, the original model in Gao et al. (2014) employs a fabric-dependent yield function, which is used to get a non-coaxial flow rule. This yield function creates some difficulty for explicit integration of the model (Sloan, 1987; Zhao et al., 2005), especially the detection of the yield surface intersection under complex loading conditions. To overcome this difficulty, a yield function expressed in terms of the stress invariants is used, and a separate fabric-dependent plastic potential is employed, which is similar to the yield function in Gao et al. (2014). It is found that this change has small influence on the model predictions but can facilitate the model implementation. The main model formulations for the model will be given in this section.

The yield function of the model is expressed as

$$f = R/g(\theta) - H = 0 \tag{1}$$

where $R = \sqrt{3r_{ij}r_{ij}/2}$, with $r_{ij} = \left(\sigma_{ij} - p\delta_{ij}\right)/p$ being the stress ratio tensor, in which σ_{ij} is the stress tensor, $p = \sigma_{ii}/3$ is the mean normal stress; δ_{ij} $(= 1$ for $i = j$, and $= 0$ for $i \neq j)$ is the Kronecker delta; H is the hardening parameter; $g(\theta)$ is an interpolation function based on the Lode angle θ of r_{ij} as follows (Li & Dafalias, 2004)

$$g(\theta) = \frac{\sqrt{(1+c^2)^2+4c(1-c^2)sin3\theta}-(1-c^2)}{2(1-c)sin3\theta} \tag{2}$$

where $c = M_e/M_c$ is the ratio between the critical state stress ratio R in triaxial extension M_e and that in triaxial compression M_c.

The plastic potential function in the r_{ij} space is expressed as

$$g = R/g(\theta) - H_g \exp[-k_h(1-A)^2] = 0 \tag{3}$$

where k_h is a model parameter, A is the anisotropic variable and H_g should be calculated based on the current stress state and A. Note that g is only used to determine the plastic deviatoric strain increment de_{ij}^p, rather than the total plastic strain increment $d\varepsilon_{ij}^p$. The anisotropic variable A is defined as

$$A = F_{ij}n_{ij} \tag{4}$$

where F_{ij} is the fabric tensor characterising the anisotropy of sand and the loading direction tensor n_{ij} is expressed by

$$n_{ij} = \frac{\frac{\partial f}{\partial r_{ij}}-\left(\frac{\partial f}{\partial r_{mn}}\delta_{mn}\right)\delta_{ij}/3}{\left\|\frac{\partial f}{\partial r_{ij}}-\left(\frac{\partial f}{\partial r_{mn}}\delta_{mn}\right)\delta_{ij}/3\right\|} \tag{5}$$

More details of the definition of F_{ij} can be found in Li and Dafalias (2012), Gao et al. (2014) and Gao and Zhao (2013). For the present study, the initial F_{ij} is given in Eq. (15) below. The value of A varies between -1 and 1. The plastic potential function in Eq. (3) is used to get the direction of plastic deviatoric strain increment de_{ij}^p as below

$$de_{ij}^p = \langle L\rangle m_{ij}, \text{ with } m_{ij} = \frac{\frac{\partial g}{\partial r_{ij}}-\left(\frac{\partial g}{\partial r_{mn}}\delta_{mn}\right)\delta_{ij}/3}{\left\|\frac{\partial g}{\partial r_{ij}}-\left(\frac{\partial g}{\partial r_{mn}}\delta_{mn}\right)\delta_{ij}/3\right\|} \tag{6}$$

where L is the loading index; $\langle\ \ \rangle$ are the Macaulay brackets ($\langle L\rangle = L$ for $L > 0$ and

$\langle L\rangle = 0$ for $L \leq 0$). It is shown by in Gao et al. (2014) and Zhao and Gao (2016) that the flow rule expressed by Eq. (6) can capture the non-coaxial sand response in monotonic loading caused by fabric anisotropy. The total plastic strain increment $d\varepsilon_{ij}^{p}$ is (Zhao and Gao, 2016)

$$d\varepsilon_{ij}^{p} = de_{ij}^{p} + \frac{1}{3} d\varepsilon_{v}^{p}\delta_{ij} = \langle L\rangle\left(m_{ij} + \sqrt{\frac{2}{27}} D\delta_{ij}\right) = \langle L\rangle \mathrm{N}_{ij} \tag{7}$$

where N_{ij} is self-evident, $d\varepsilon_{v}^{p}$ is the plastic volumetric strain increment and D is the dilatancy relation expressed as

$$D = \frac{d\varepsilon_{v}^{p}}{d\varepsilon_{q}^{p}} = \frac{d\varepsilon_{v}^{p}}{\sqrt{\frac{2}{3} de_{ij}^{p} de_{ij}^{p}}} = \frac{d_1}{M_c g(\theta)}\left[M_c g(\theta) e^{m\zeta} - R\right] \tag{8}$$

$$\zeta = \psi - e_A(A-1) \tag{9}$$

where d_1, m and e_A are three model parameters; ζ is the dilatancy state parameter (Li and Dafalias, 2012); ψ $(= e - e_c)$ is the state parameter (Been and Jefferies, 1985), with e_c being the critical state void ratio corresponding to the current p. The critical state line in the $e-p$ plane is given by (Li and Wang, 1998)

$$e_c = e_\Gamma - \lambda_c (p/p_a)^{\xi} \tag{10}$$

where e_Γ, λ_c and ξ are three material constants and p_a is the atmospheric pressure (101 kPa).

The hardening law for the yield function (evolution of for H) is expressed as

$$dH = \langle L\rangle r_H = \frac{G h_1 e^{h_2 A}}{(1+e)^2 \sqrt{p p_a} R}\left[M_c g(\theta) e^{-n\zeta} - R\right] \tag{11}$$

where h_1, h_2 and n are three model parameters and G is the elastic shear modulus, the expression for which will be given below. The term $e^{h_2 A}$ is introduced to give better prediction for the effect of anisotropy on stress-strain relationship, which makes the plastic modulus smaller at smaller A (Li and Dafalias, 2012; Papadimitriou et al., 2019).

Fabric evolution with plastic deformation is considered in the model. It is assumed that F_{ij} becomes co-directional with the loading direction n_{ij} and reaches a magnitude of 1 at the critical state. Though fabric evolution is affected by both volumetric and shear strain, a simplified evolution law expressed in terms of the plastic shear strain as below is used

$$dF_{ij} = \langle L \rangle k_f \left(n_{ij} - F_{ij} \right) \tag{12}$$

where k_f is a model parameter.

The following empirical pressure-sensitive elastic moduli are employed for this model (Li and Dafalias, 2000; Gao et al., 2014):

$$G = G_0 \frac{(2.97-e)^2}{1+e} \sqrt{p p_a} \qquad \text{and} \qquad K = G \frac{2(1+\nu)}{3(1-2\nu)} \tag{13}$$

where G_0 is a material constant and ν is the Poisson's ratio. In conjunction with Eq. (13), the following hypoelastic stress-strain relationship is assumed for calculating the incrementally reversible deviatoric and volumetric strain increments de_{ij}^e and $d\varepsilon_v^e$:

$$de_{ij}^e = \frac{ds_{ij}}{2G} \quad \text{and} \quad d\varepsilon_v^e = \frac{dp}{K} \tag{14}$$

Model implementation

This model has been implemented in the finite element package ABAQUS through the user-material (UMAT) interface using an explicit integration method (Sloan, 1987; Zhao et al., 2005; Jin et al., 2017; Jin et al., 2018). To increase the efficiency for global equilibrium iteration, the secant modulus for each step is stored at the end of each strain increment here. The large strain formulation proposed by Hughes and Winget (1980) (see also ABAQUS User Manual) is employed in the implementation. The plane strain and triaxial compression test data on Toyoura sand reported in Oda et al. (1978), Fukushima and Tatsuoka (1984) and Tatsuoka et al. (1986) is used to benchmark the model simulations for single element soil response, as the centrifuge tests to be simulated in this study (Kimura et al., 1985) have used similar sample preparation methods. The model parameters are listed in Table 1. Determination of these parameters have been discussed in Gao et al. (2014). The parameters for the critical state can be readily determined based on the critical state stress ratio and critical state line location. The elasticity parameters are determined using the stress-strain relationship at low strain level. The remaining ones are obtained via a trial-and-error approach. But our experience shows that there is a certain range for these parameters, which can be used as initial values for the determination process. It is noticed that the Bayesian-based parameter identification is a more efficient and powerful approach for getting these parameters, which will be pursued in the future (Yin et al., 2018; Jin et al., 2018; Jin et al., 2019).

Comparison between the model simulations (lines) and test data (dots) on Toyoura sand under various loading conditions is shown in Figs. 1-3. The initial degree of anisotropy is chosen as $F_0 = 0.35$. This is an estimated value as it is generally difficult to measure F_0. One may use the undrained effective stress path to calculate F_0 using anisotropic elasticity (Zhao and Gao, 2016). But such data is not available. In this study, horizontal and vertical samples have horizontal and vertical bedding planes, respectively. Samples with horizontal bedding are used in the triaxial compression tests. The model gives good prediction on the peak deviator stress but does not capture the strain softening part well. While the model may need to be improved to get better predictions, the stress-strain relationship after the peak deviator stress may not represent the real soil response due to strain localization (Oda et al., 1978; Huang et al., 2010).

Finite element modelling of a strip footing response on sand

Simulation of the centrifuge tests

The centrifuge test data reported in Kimura et al. (1985) is used to benchmark the model simulation of a real footing problem. The prototype size of the footing is used in the simulations (Fig. 4), which is similar to the approach adopted by Chaloulos et al. (2019). As the size of the soil box used in the centrifuge tests is not reported in Kimura et al. (1985), the height and width of the soil body are assumed, which are big enough to eliminate the boundary effect on the footing response. Simulations with different sizes of soil mass have been performed. It is found that there is negligible soil movement and stress change at the boundary at the current soil mass size during loading. The $\frac{s}{B} - Q$ is relationship does not change if bigger soil mas is used (see Fig. 5), where s is the vertical footing settlement, B is the footing length and Q is the vertical pressure applied on the footing. Due to the non-coaxial deformation predicted by the constitutive model, the stress and deformation field in the soil may not be symmetric. Therefore, it is not proper to use only half of the soil body for the simulations (Azami et al., 2010; Kawamura and Muira, 2014). The force and displacement relationship of the footing is mainly affected by the soil elements around it, and therefore, a semicircle with finer mesh is created beneath it (Fig. 4). Eight-node quadratic plane strain elements with reduced integration are used. Uniform vertical pressure of 1kPa is applied on the top surface of the sand to avoid soil collapse with zero mean effective stress. Uniform vertical deformation is applied in the footing area, which means that the relative movement between footing and sand is neglected. No horizontal or vertical movement is allowed at the bottom of soil body while only horizontal movement is restricted at the two vertical sides. As there is no water in the sand, $\gamma = \gamma' = 16\mathrm{kN/m^3}$ is used according to Oda and Koishikawa (1979), where γ and γ' denote the bulk and effective unit weight, respectively. The initial lateral earth pressure coefficient is assumed to be the same for all cases with $K_0 = 0.4$ (Okochi and Tatsuoka, 1984). The maximum and minimum void ratios for Toyoura sand are $e_{max} = 0.98$ and $e_{min} = 0.6$. Since the initial stress state is anisotropic for sand beneath the footing, a value of initial degree of anisotropy ($F_0 = 0.4$) higher than that for the plane strain test samples with initially isotropic stress state is assumed. The initial fabric for the soil is assumed the same for the entire soil. When the bedding plane is horizontal, it is given using the equation below

$$F_{ij} = \begin{pmatrix} F_{xx} & F_{xy} & F_{xz} \\ F_{yx} & F_{yy} & F_{yz} \\ F_{zx} & F_{zy} & F_{zz} \end{pmatrix} = \sqrt{\frac{2}{3}} \begin{pmatrix} -F_0/2 & 0 & 0 \\ 0 & F_0 & 0 \\ 0 & 0 & -F_0/2 \end{pmatrix} \tag{15}$$

with z-direction being perpendicular to the x-y plane. When the bedding plane is not horizontal, orthogonal transformation of Eq. (15) has to been carried out (Gao et al., 2014).

The finite element simulation result is dependent on the mesh size and orientation, as the model uses non-associated flow rule and gives strain-softening response in some cases. Following Chaloulos et al. (2019), different mesh sizes in the semicircle area were used to simulate the three cases in Fig. 5 and the mesh size which gives the best prediction for the bearing capacity is chosen (Fig. 4). The mesh size outside the semicircle has negligible influence on the force and displacement relationship. The same mesh is used in all the simulations in this study.

Fig. 5 shows the simulations for the centrifuge tests on sand reported in Kimura et al. (1985). In this and the following figures, B is the footing width. In each group of tests, sand samples with horizontal ($\alpha = 0^{\mathrm{o}}$ in Fig. 4) and vertical ($\alpha = 90^{\mathrm{o}}$ in Fig. 4) bedding planes are used.

Note that the force and displacement relationships beyond $s/B = 0.25$ are not shown in most of the figures in this paper, because there is significant distortion of elements near the footing edges in some simulated tests, which makes the results unreliable. Higher bearing capacity Q_u, which is the peak value of Q, is observed for relatively dense sand ($D_r \approx 86\%$ and $D_r \approx 75\%$) with horizontal bedding (Figs. 5a and b). The difference is about 12.5% for $D_r \approx 86\%$ and 10% for $D_r \approx 75\%$. But the effect of bedding plane orientation on Q_u becomes negligible when $D_r \approx 62\%$ (Fig. 5c), which is consistent with the small model test results in Oda and Koishikawa (1979). For all the tests, sand with horizontal bedding show smaller settlement at the same Q before failure. The simulations give good prediction for the bearing capacity in all three cases. The simulated settlement before failure (peak Q or Q_u) is larger than the measured one for horizontal bedding, especially for the dense sand in Fig. 5a. The initial slope of the $s/B - Q$ curves predicted by the model is also smaller than the measured one for horizontal bedding. The discrepancy between simulations and test results could be caused by the model itself. First, the yield surface for this model does not consider the sand yielding due to pure compression without change in the stress ratio; Secondly, the small strain stiffness of sand is not accounted for. But the nonuniformity of sand samples and mesh size may have also contributed (Oda et al., 1978; Oda and Koishikawa, 1979; Azami et al., 2010). Overall, the model gives reasonable description for the effect of density and anisotropy on the bearing capacity of strip footings.

Failure mechanism of sand under the strip footing

Progressive failure is observed in all the simulations. The numerical simulations indicate that shear strain localization initiates at the peak Q states and two clear slip lines (or shear bands) develop at sufficiently large s/B for dense and medium dense sand ($D_r > 45\%$) with various bedding plane orientations, which agrees with the 1g model test and centrifuge test observations (Kimura et al., 1985; Kawamura and Muira, 2014). In this case, the soil elements fail progressively on the slip lines, with those under the footing centre failing first. This is called the general shear failure mode (Vesic, 1963; Lau and Bolton, 2011). When $D_r < 45\%$, no clear slip lines develop in sand and the failure mode is close to the punching shear (Vesic, 1963; Lau and Bolton, 2011), where only the elements on two sides of a soil wedge beneath the footing fail (Lau and Bolton, 2011). Similar simulation results have been reported in Loukidis and Salgado (2011).

Two groups of tests with different sand densities are used to illustrate the general shear failure, with the force and displacement relationships for footings being shown in Fig. 6. The definition of α is shown in Fig. 4. The peak and residual Q states in Figs. 6-8 are respectively denoted by 'P*x*' and 'R*x*', where the number '*x*' represent the bedding plane orientation in degrees. Figs. 7 and 8 show the contour of incremental shear strain at the peak and residual Q states for these simulations. The incremental shear strain $\delta\varepsilon_q$ is defined as

$$\delta\varepsilon_q = \sqrt{\frac{2}{3}\delta e_{ij}\delta e_{ij}} \tag{16}$$

where δe_{ij} is the increment of deviatoric strain for each step. Note that the patterns of total shear strain contours and incremental shear strain contours at residual states are similar for these tests. At $D_r = 86\%$, the depth of the slip lines is the biggest at $\alpha = 0^{\circ}$ and smallest at $\alpha = 90^{\circ}$, which agrees well with the centrifuge tests (Kimura et al., 1985). But there is no significant difference in the slip line depth at different α values for test simulations with $D_r = 70\%$. In addition, the slip lines are symmetric when $\alpha = 0^{\circ}$ and $\alpha = 90^{\circ}$, because the initial soil fabric is symmetric about the middle of the soil body, which makes the displacement field in sand symmetric and the total reaction force on the footing vertical (Fig. 9a). On the other hand, unsymmetrical slip lines are predicted at $\alpha = 45^{\circ}$, which has also been observed in the model tests by Kawamura and Muira (2014). This is due to that the non-coaxial sand response makes the displacement field unsymmetrical, which is shown in Fig. 9b. More discussion on this can be found in Gao and Zhao (2013). If the horizontal displacement of the footing were not restricted, the footing would move to the right (positive *x* direction in Fig. 4) due to such displacement. In the present study, however, the horizontal movement of the footing is fixed, which means that there is horizontal reaction force (pointing to the negative *x* direction) on the footing due to this restriction. The total reaction force F on the footing thus aligns in the direction shown in Fig. 9b, which renders the soil swell more on the left (Figs. 7d and 8d). Indeed, unsymmetrical slip lines have also been observed in model and centrifuge tests with horizontal bedding plane (Kimura et al., 1985; Kawamura and Miura, 2014). This has frequently been interpreted as the consequence of nonuniform void ratio distribution (e.g., Nübel and Huang, 2004; Bauer et al., 2004). However, this could be associated with fabric anisotropy as well. Though the bedding plane is horizontal in an average sense, the local soil fabric may vary at different locations, which makes the displacement field unsymmetrical (Guo and Zhao, 2016).

One test with horizontal bedding is used to illustrate the punching shear failure mode ($D_r =$ 30%). The force and displacement relationship for this test is shown in Fig. 10, in which no obvious peak Q can be observed. Fig. 11 shows the failure mechanism for this test. The incremental shear strain contour at s/B=0.25 indicates the development of a soil wedge beneath the footing. As the vertical displacement increases, the incremental shear strain concentrates more at the two footing edges, without extending laterally. At s/B=0.4, a fully developed soil wedge can be observed, with intensive shear strain concentration on the two sides (Fig. 11b). Though the shear strain localization extends a little beyond the soil wedge, clear slip lines do not form, which is different from the general shear failure (Vesic, 1963; Lau and Bolton, 2011).

Vanishing effect of α on the bearing capacity of strip footings Q_u

Existing 1g model and centrifuge tests on Toyoura sand show that the effect of α on Q_u becomes negligible when D_r <70%, though the settlement at the same Q is still larger at bigger α before Q_u (Oda et al., 1978; Kimura et al., 1985). Fig. 12 shows the simulated variation of Q_u with D_r for Toyoura sand with horizontal and vertical bedding. Small difference between the Q_u for the two bedding plane orientations can be observed when D_r ≤70%, while the difference in settlement at the same Q still exists (e.g., Fig. 6b). Note that there is no obvious peak Q in three of the simulated tests ($D_r = 60\%$ with vertical bedding, and $D_r = 55\%$ with both vertical and horizontal bedding), and therefore, alternative methods have to be used for estimating Q_u. Vesic (1963) recommends using the value of Q at the fastest rate of settlement with respect to time, which is typically difficult to obtain. In this study, Q at $s/B \approx 0.2$ is defined as Q_u, because localized failure and peak Q can be observed at this settlement level for relatively loose sand in a real test (Kimura et al., 1985).

The similarity in Q_u seems counter-intuitive, because the effect of anisotropy on shear strength, stiffness and dilatancy of single sand elements can be observed for any soil densities (e.g., Tatsuoka et al., 1986; Yang et al., 2008; Gao et al., 2014). Fig. 13 shows the response of sand elements about 1B beneath the centre of the footings (Element A in Fig. 4) for four of the simulations in Fig. 6. Element A is chosen because it is on the slip lines for all the simulated tests and has direct influence on Q_u. It is evident that the soil elements show smaller normalized peak stress ratio $R/[M_c g(\theta)]$ and less volume expansion at $\alpha = 90^{\circ}$ for two different densities, which is consistent with the laboratory test observations. Therefore, the difference in Q_u caused by α cannot be solely attributed to the shear strength anisotropy of sand elements. The failure mechanism of sand beneath the strip footings must play an important role as well. When the sand density is high (e.g., $D_r = 86\%$ in Fig. 6a), progressive failure initiates at similar settlement level (corresponding to Q_u), though different, for different bedding plane orientations, and the strength anisotropy of sand elements governs the Q_u. At lower sand density (e.g., $D_r = 70\%$ in Fig. 6b), progressive failure in sand with horizontal bedding initiates at much higher settlement compared to the counterpart with horizontal bedding. Delayed progressive failure has allowed the external load to be distributed more evenly in the soil. Some previous studies have assumed that Q_u is only dependent on the peak friction angle of sand elements (Meyerhof, 1978; Siddiquee et al., 1999) but independent of the failure mechanism. Such assumption cannot explain the similarity in Q_u for the tests shown in Fig. 12.

Response of strip footings on sand with horizontal bedding: combined effect of density and F_0

Discussions in the previous sections have mainly showed how the bedding plane orientation affects the response of strip footings. But footings on sand with horizontal bedding are of greater importance for practical applications, which will be the focus of this section. The main objective is to investigate the combined effect of sand density and F_0 and identify which of them plays more important role in governing the bearing capacity and failure mechanism of strip footings.

Fig. 14 shows the effect of relative density on the force and displacement relationship of strip footings. Two values of F_0 (0 and 0.4) are used in the simulations to represent different soil compaction methods in the engineering practice, because it is shown in Zhao and Gao (2016) that the stress-strain relationship of sand samples prepared using different methods can be simulated with different F_0. Some research [e.g., Yang et al., (2008)] has shown that about 3 of the model parameters may have to be adjusted to get quantitative prediction of the soil response. But qualitative results for the effect of compaction methods are sufficient for this study. There is obvious peak Q for simulations with $D_r = 90\%$ and $D_r = 70\%$, which is considered as the bearing capacity (Q_u). But Q keeps increasing with s/B for sand with $D_r = 50\%$ and $D_r = 30\%$. Same as the previous section, Q corresponding to s/B=0.2 is defined as Q_u for these tests. For both F_0 values, dramatic influence of relative density on the bearing capacity is observed. Q_u at $D_r = 90\%$ is almost 6 times of that at $D_r = 30\%$ for both F_0 values. The failure mechanism is found independent of F_0.

Fig. 15 shows the effect of F_0 on the response of strip footings. At $D_r = 80\%$, Q_u decreases as F_0 increases, which indicates that Q_u is higher when the soil is more isotropic. This is attributable to the distribution of anisotropic variable A in the sand. F_0 can affect Q_u by about 20% for $D_r = 80\%$ and by about 45% for $D_r = 50\%$. Fig. 16 shows the variation of A in sand at s/B=0.11 (close to the Q_u state) for initially isotropic and anisotropic fabric cases with $D_r = 80\%$. For the case with initially isotropic fabric, the value of A lies between 0.01 and 0.02 in the area beneath the footing and is about 0 in the remaining area (Fig. 16a). This indicates rather uniform distribution of A. Very ununiform distribution of A is observed for the simulation with $F_0 = 0.6$ (Fig. 16b). The maximum A is between 0.4 and 0.6 (beneath the footing) and the minimum A is about -0.3 (beside the two edges of the footing). For both cases, the stress state and void ratio for all the elements at this deformation level is similar. Based on the model formulations, one can see that higher A indicates bigger r_H and higher shear resistance under otherwise identical conditions of stress and void ratio. Therefore, the sand elements beneath the footing have lower shear resistance when $F_0 = 0$ (A is lower in that area compared to the case with $F_0 = 0.6$), but they are supported by elements with higher shear resistance (bigger A for elements under the two edges of the footing). This eventually leads to higher bearing capacity of the footing. Such difference in distribution of A can also explain why the force-displacement curves for more isotropic sand lie higher beyond $\frac{s}{B} = 0.7$ when $D_r = 50\%$ (Fig. 15b). The failure mechanism of sand under the footing is mainly controlled by the sand density.

It can be seen from Figs. 14 and 15 that the sand density plays a more dominant role in controlling the bearing capacity and failure mechanism of strip footings. A small variation of D_r can result in a big change in Q_u. Though F_0 affects Q_u as well, this influence is smaller compared to the effect of D_r (Gao et al., 2014; Chaloulos et al., 2019). However, this does not mean that fabric anisotropy should be neglected in modelling the response of strip footings. If an isotropic model is used, Q_u can be significantly overestimated, which will be discussed in the next Section.

Prediction of the strip footing response by an isotropic model

The previous section shows that the influence of F_0 on Q_u is smaller than that of D_r. But this does not mean that fabric anisotropy should be neglected in modelling the bearing capacity of strip footings. The soil fabric will become anisotropic when it is subjected to external loading, even though it is initially isotropic. Therefore, the effect of fabric anisotropy on soil response is present for an initially isotropic soil sample. To show the importance of considering fabric anisotropy in describing the response of strip footings on sand, prediction of the isotropic model will be given below.

The parameters for the isotropic model are determined using drained triaxial compression tests and plane strain compression tests on sand with horizontal bedding (Figs. 17 and 18). All the parameters are shown in Table 2, with those associated with fabric anisotropy set 0 (see also Chaloulos et al., 2019). The model gives good prediction for triaxial compression test data. For plane strain tests, the model does not capture the softening part well, as strain localization in the sample makes the decreasing of deviator stress more dramatic.

Prediction of the isotropic model (lines) for the centrifuge test data (dots) with horizontal bedding are shown in Fig. 19. The same mesh and boundary conditions shown in Fig. 4 are used. The model overestimates the Q_u dramatically. For the tests with $D_r = 64.6\%$ and $D_r = 75.1\%$, the predicted Q_u is almost twice of the measured one. At $D_r = 85.6\%$, the isotropic model gives about 50% overestimation of Q_u. This indicates that fabric anisotropy must be properly considered in modelling the strip footing response on sand, which is consistent with the conclusion in Chaloulos et al., (2019). The main reason for this overestimation is that the isotropic model gives too high shear strength for elements with non-vertical major principal stress direction under the footing (Tatsuoka et al., 1986).

Conclusions

This paper presents a new numerical study on the fabric effect on bearing capacity and failure mechanism of strip footings on anisotropic sand. A critical state sand model accounting for fabric evolution is used. It employs a non-coaxial flow rule which is expressed in terms of the current state of stress and fabric. The model is validated against both element and centrifuge tests on Toyoura sand. The following conclusions can be drawn from the study:

(a) The bearing capacity Q_u of strip footings on sand with different bedding plane orientation α is governed by not only the strength anisotropy of sand elements but also the failure mechanism of soil body. Strength anisotropy of sand elements has more influence on Q_u when the sand density is high, making Q_u higher when the bedding plane is horizontal. The difference in Q_u caused by α vanishes at lower sand density (e.g., $D_r \leq 70\%$ for Toyoura sand), as progressive failure initiates at larger settlement for sand with vertical bedding plane, which allows the external loading to be distributed more evenly in the soil. Irrespective the sand density, the settlement of footings at the same Q increases as α increases before Q_u.

(b) Progressive failure is predicted in all the simulations, which is supported by small-scale and centrifuge test observations. General shear failure mode is observed in dense and medium dense sand. For this failure mode, progressive failure initiates at the peak Q state and clear slip lines can be observed at large settlement. The slip lines are symmetrical when the bedding plane is horizontal or vertical. Due to the non-coaxial deformation of sand caused by fabric anisotropy, unsymmetrical slip lines develop when the bedding plane is inclined. Punching shear failure is the main failure mechanism for loose sand, where soil failure concentrates along two edges of a soil wedge beneath the footing.

(c) For strip footings in practical applications where the bedding plane is horizontal, soil density plays a more dominant role in governing the bearing capacity and failure mechanism of the soil body. At the same density, Q_u is higher when the initial sand fabric is more isotropic, because the soil beneath the footing is supported by soil with higher shearing resistance below the footing edges. The initial degree of fabric anisotropy F_0 does not have effect on development of general shear or punching shear failure.

(d) An isotropic model can give significant overestimation of Q_u of strip footings on anisotropic sand. The main reason for this overestimation is that the isotropic model gives too high shear strength for elements with non-vertical major principal stress direction under the footing (Tatsuoka et al., 1986).

This research has several implications for engineering practice: (a) It is important to realize that the bearing capacity is not only dependent on the strength anisotropy of sand but also the failure mechanism of soil body; (b) The unsymmetrical slip lines observed under strip footings could be caused by both fabric anisotropy and ununiform distribution of soil density; (c) For a typical range of F_0 and horizontal bedding, the sand density plays a more important role in governing Q_u and failure mechanism of sand. However, if an isotropic model is used, Q_u can be significantly overestimated, which is consistent with previous research findings.

Data Availability Statement

Some or all data, models, or code generated or used during the study are available from the corresponding author by request.

References

Azami, A., S. Pietruszczak, and P. Guo. 2010. “Bearing capacity of shallow foundations in transversely isotropic granular media.” *Int J Numer Anal Method Geomech*. 34 (8): 771-793. https://doi.org/10.1002/nag.827.

Bauer, E., W. Huang, and W. Wu. 2004. “Investigations of shear banding in an anisotropic hypoplastic material.” *Int J Solid Struct*. 41: 5903-5919. https://doi.org/10.1016/j.ijsolstr.2004.05.052.

Been, K., and M. G. Jefferies. 1985. “A state parameter for sands.” *Géotechnique*. 35(2): 99-112. https://doi.org/10.1680/geot.1985.35.2.99.

Chaloulos, Y. K., A. G. Papadimitriou, Y. F. Dafalias 2019. “Fabric effects on strip footing loading of anisotropic sand.” *J. Geotech. Geoenviron. Eng.* 145(10): 04019068. https://doi.org/10.1061/(ASCE)GT.1943-5606.0002082.

Chang, C. S., and Z. Y. Yin. 2009. “Micromechanical modeling for inherent anisotropy in granular materials.” *J. Eng. Mech.* 136(7): 830-839.

Dafalias, Y. F., A. G. Papadimitriou, and X.-S. Li. 2004. “Sand plasticity model accounting for inherent fabric anisotropy.” *J. Eng. Mech.* 130 (11): 1319-1333. https://doi.org/10.1061/(ASCE)0733-9399(2004)130:11(1319).

Fu, P.-C., and Y. F. Dafalias. 2011. “Study of anisotropic shear strength of granular materials using DEM simulation.” *Int. J. Numer. Anal. Meth. Geomech.* 35: 1098-1126. https://doi.org/10.1002/nag.945.

Fukushima, S., and F. Tatsuoka. 1984. “Strength and deformation characteristics of saturated sand at extremely low pressures.” *Soils Found.* 24(4): 30-48. https://doi.org/10.3208/sandf1972.24.4_30.

Gao, Z., J. Zhao, X.-S. Li, and Y. F. Dafalias 2014. “A critical state sand plasticity model accounting for fabric evolution.” *Int. J. Numer. Anal. Meth. Geomech.* 38(4): 370-390. https://doi.org/10.1002/nag.2211.

Gao, Z., and J. Zhao. 2013. “Strain localization and fabric evolution in sand.” *Int. J. Solid. Struct*. 50: 3634-3648. https://doi.org/10.1016/j.ijsolstr.2013.07.005.

Guo, N., and J. Zhao. 2013. “The signature of shear-induced anisotropy in granular media.” *Comput. Geotech.* 47: 1-15. https://doi.org/10.1016/j.compgeo.2012.07.002.

Guo, N., and J. Zhao. 2016. “3D multiscale modelling of strain localization in granular media.” *Comput. Geotech.* 80: 360-372. https://doi.org/10.1016/j.compgeo.2016.01.020.

Guo, P. 2008. “Modified direct shear test for anisotropic strength of sand.” *J. Geotech. Geoenviron. Eng.* 134(9): 1311-1318. https://doi.org/10.1061/(ASCE)1090-0241(2008)134:9(1311).

Huang, M., X. Lu, Lu, J. Qian. 2010. “Non-coaxial elasto-plasticity model and bifurcation prediction of shear banding in sands.” *Int. J. Numer. Anal. Meth. Geomech.* 34(9): 906-919. https://doi.org/10.1002/nag.838.

Hughes, T. J. R., and J. Winget. 1980. “Finite rotation effects in numerical integration of rate constitutive equations arising in large deformation analysis.” *Int. J. Numer. Meth Eng.* 15: 1862-1867. https://doi.org/10.1002/nme.1620151210.

Jin, Y. F., Z. X. Wu, Z. Y. Yin, and J. S. Shen. 2017. “Estimation of critical state-related formula in advanced constitutive modeling of granular material.” *Acta Geotechnica*, 12(6): 1329-1351.

Jin, Y. F., Z. Y. Yin, Z. X. Wu, and A. Daouadji. 2018. “Numerical modeling of pile penetration in silica sands considering the effect of grain breakage.” *Fin. Elem. Analy. Desig.* 144: 15-29.

Jin, Y. F., Z. Y. Yin, Z. X. Wu, and W. H. Zhou. 2018. “Identifying parameters of easily crushable sand and application to offshore pile driving.” *Ocean Eng.* 154: 416-429.

Jin, Y. F., Z. Y. Yin, W. H. Zhou, and S. Horpibulsuk. 2019. “Identifying parameters of advanced soil models using an enhanced transitional Markov chain Monte Carlo method.” *Acta Geotech.* 14(6): 1925-1947.

Kawamura, S., and S. Miura. 2014. “Bearing capacity improvement of anisotropic sand ground.” *Proceed. Instit. Civil Engi. - Ground Improvement*, 167(3), 192-205. https://doi.org/10.1680/grim.13.00011.

Kimura, T, O. Kusakabe O, and K. Saitoh. 1985. “Geotechnical model tests of bearing capacity problems in a centrifuge.” *Géotechnique*. 35(1): 33-45. https://doi.org/10.1680/geot.1985.35.1.33.

Lau, C. K., and M. D. Bolton 2011. “The bearing capacity of footings on granular soils. II: Experimental evidence.” *Géotechnique*. 61(8): 639-650. https://doi.org/10.1680/geot.7.00207.

Li, X.-S., and Y. F. Dafalias. 2004. “A constitutive framework for anisotropic sand including non-proportional loading.” *Géotechnique*. 54 (1): 41-55. https://doi.org/10.1680/geot.2004.54.1.41.

Li, X.-S., and Y. F. Dafalias. 2012 “Anisotropic critical state theory: the role of fabric.” *J. Eng. Mech.* 138 (3): 263-275. https://doi.org/10.1061/(ASCE)EM.1943-7889.0000324.

Li, X.-S., and X. Li. 2009. “Micro-Macro quantification of the internal structure of granular materials.” *J. Eng. Mech.* 135 (7): 641-656. https://doi.org/10.1061/(ASCE)0733-9399(2009)135:7(641).

Li, X.-S., and Y. Wang. 1998. “Linear representation of steady-state line for sand.” *J. Geotech. Geoenviron. Eng.* 124 (12): 1215-1217. https://doi.org/10.1061/(ASCE)1090-0241(1998)124:12(1215).

Loukidis, D., and R. Salgado. 2011. “Effect of relative density and stress level on the bearing capacity of footings on sand.” *Géotechnique*. 61(2): 107-119. https://doi.org/10.1680/geot.8.P.150.3771.

Meyerhof, G. G. 1978. “Bearing capacity of anisotropic cohesionless soils.” *Can. Geotech. J.* 15(4): 592-595. https://doi.org/10.1139/t78-063.

Miura, S., and S. Toki. 1982. “A sample preparation method and its effect on static and cyclic deformation-strength properties of sand.” *Soils Found.* 22(1): 61-77. https://doi.org/10.3208/sandf1972.22.61.

Nemat-Nasser, S., and J. Zhang. 2002. “Constitutive relations for cohesionless frictional granular materials.” *Int. J. Plast.* 18: 531-547. https://doi.org/10.1016/S0749-6419(01)00008-0.

Nübel, K., W. Huang 2004. “A study of localized deformation pattern in granular media.” *Comput. Meth. Appl. Mech. Eng.* 193(27-29): 2719-2743. https://doi.org/10.1016/j.cma.2003.10.020.

Oda, M., and H. Kazama. 1998. “Microstructure of shear bands and its relation to the mechanisms of dilatancy and failure of dense granular soils.” *Géotechnique*. 48: 465-481. https://doi.org/10.1680/geot.1998.48.4.465.

Oda, M., I. Koishikawa, and T. Higuchi. 1978. “Experimental study of anisotropic shear strength of sand by plane strain test.” *Soils Found.* 18(1): 25-38. https://doi.org/10.3208/sandf1972.18.25.

Oda, M., and I. Koishikawa. 1979. “Effect of strength anisotropy on bearing capacity of shallow footing in a dense sand.” *Soils Found.* 19(3): 15-28. https://doi.org/10.3208/sandf1972.19.3_15.

Okochi, Y., and F. Tatsuoka. 1984. “Some factors affecting K_0-values of sand measured in triaxial cell.” *Soil Found.* 24(3): 52-68. https://doi.org/10.3208/sandf1972.24.3_52.

Papadimitriou, A. G., Y. K. Chaloulos, and Y. F. Dafalias. 2019. “A fabric-based sand plasticity model with reversal surfaces within anisotropic critical state theory.” *Acta Geotech.* 14 (2): 253-277. https://doi.org/10.1007/s11440-018-0751-5.

Siddiquee, M. S. A., T. Tanaka, F. Tatsuoka, K. Tani, and T. Morimoto T. 1999. Numerical simulation of bearing capacity characteristics of strip footing on sand. *Soils Found.* 39(4): 93-109. https://doi.org/10.3208/sandf.39.4_93.

Sloan, S. W. 1987. “Substepping schemes for the numerical integration of elastoplastic stress-strain relations.” *Int. J. Numer. Meth. Eng.* 24 (5): 893-911. https://doi.org/10.1002/nme.1620240505.

Tatsuoka, F., M. Sakamoto, T. Kawamura, and S. Fukushima. 1986. “Strength and deformation characteristics of sand in plane strain compression at extremely low pressures.” *Soils Found.* 26(1), 65-84. https://doi.org/10.3208/sandf1972.26.65.

Tejchman, J., and J. Górski. 2010. “Finite element study of patterns of shear zones in granular bodies during plane strain compression.” *Acta Geotech.* 5: 95-112.

Thornton, C., and L. Zhang. 2010. “On the evolution of stress and microstructure during general 3D deviatoric straining of granular media.” *Géotechnique*. 60(5): 333-341. https://doi.org/10.1680/geot.2010.60.5.333.

Vesic, A. S. 1963. “Bearing capacity of deep foundations in sand.” *Highway Research Record.* 39: 112-153.

Wan, R. G., and P. J. Guo. 2001. “Effect of microstructure on undrained behaviour of sands.” *Can. Geotech. J.* 38(1): 16-28. https://doi.org/10.1139/cgj-38-1-16.

Yang, Z-.X., X.-S. Li, and J. Yang. 2008. “Quantifying and modelling fabric anisotropy of granular soils.” *Géotechnique*. 58(4): 237-248. https://doi.org/10.1680/geot.2008.58.4.237.

Yin, Z. Y., C. S. Chang, and P. Y. Hicher. 2010. “Micromechanical modelling for effect of inherent anisotropy on cyclic behaviour of sand.” *Int. Solids Struct.* 47(14-15): 1933-1951.

Yin, Z. Y., Y. F. Jin, J. S. Shen, and P. Y. Hicher. 2018. “Optimization techniques for identifying soil parameters in geotechnical engineering: comparative study and enhancement.” *Int. J. Numer. Method. Geomech.* 42(1): 70-94.

Yin, Z. Y., J. Zhao, and P. Y. Hicher. 2014. “A micromechanics-based model for sand-silt mixtures.” *Int. J. Solids Struct.* 51(6): 1350-1363.

Yuan, R., H.-S. Yu, N. Hu, and Y. He. 2018. “Non-coaxial soil model with an anisotropic yield criterion and its application to the analysis of strip footing problems.” *Comput. Geotech.* 99: 80-92. https://doi.org/10.1016/j.compgeo.2018.02.022.

Zhao, J. D., and Z. Gao. 2016. A unified anisotropic elasto-plastic model for sand. *J. Eng. Mech.* 142(1): 04015056. https://doi.org/10.1061/(ASCE)EM.1943-7889.0000962.

Zhao, J. D., D. C. Sheng, M. Rouainia, and S. W. Sloan. 2005. “Explicit stress integration of complex soil models.” *Int. J. Numer. Anal. Meth. Geomech.* 29: 1209-1229. https://doi.org/10.1002/nag.456.

Zhao, C. F., Z. Y. Yin, and P. Y. Hicher. 2018. “Integrating a micromechanical model for multiscale analyses.” *Int. J. Numer. Meth. Eng.* 114(2): 105-127.

List of Tables

Table 1

Elasticity	Plasticity	Critical state	Fabric effect
$G_0 = 125$ $\nu = 0.1$	$k_h = 0.03$ $n = 2.0$ $h_1 = 0.45$ $h_2 = 0.5$ $d_1 = 1.0$ $m = 3.5$	$M_c = 1.25$ $c = 0.75$ $e_\Gamma = 0.934$ $\lambda_c = 0.019$ $\xi = 0.7$	$k_f = 0.5$ $e_A = 0.075$

Table 2

Elasticity	Plasticity	Critical state	Fabric effect
$G_0 = 125$ $\nu = 0.1$	$k_h = 0$ $n = 1.5$ $h_1 = 0.6$ $h_2 = 0$ $d_1 = 0.8$ $m = 2.5$	$M_c = 1.25$ $c = 0.75$ $e_\Gamma = 0.934$ $\lambda_c = 0.019$ $\xi = 0.7$	$k_f = 0$ $e_A = 0$

List of Figure Captions

Fig. 1 Model simulation for plane strain tests on dense Toyoura sand with horizontal and vertical bedding: (a) and (b) σ_3=50 kPa; (c) and (d) σ_3=200 kPa (data from Oda et al., 1978)

Fig. 2 Comparison between the model simulations and plane strain test data on Toyoura sand with different density and confining pressure: (a) and (b) σ_3=5 kPa; (c) and (d) σ_3=400 kPa (data from Tatsuoka et al., 1986)

Fig. 3 Comparison between the model simulation and drained triaxial compression test data on Toyoura sand: (a) and (b) dense sand; (c) and (d) Medium dense sand (data from Fukushima and Tatsuoka, 1984)

Fig. 4 Size of the soil body and mesh for simulations

Fig. 5 Comparison between the centrifuge test data and finite element simulations for the force-displacement relationships of sand with different relative densities and bedding plane orientation (data from Kimura et a., 1985)

Fig. 6 The force-displacement relationship for a strip footing on sand with different bedding plane orientation: (a) $D_r = 86\%$ and (b) $D_r = 70\%$

Fig. 7 Contours of the incremental shear strain for sand with $D_r = 86\%$

Fig. 8 Contours of the incremental shear strain for sand with $D_r = 70\%$

Fig. 9 Displacement magnitude contour for sand with $D_r = 86\%$: (a) $\alpha = 0^{\mathrm{o}}$, $s/B = 0.2$; (b) $\alpha = 45^{\mathrm{o}}$ at $s/B = 0.21$

Fig. 10 The force displacement relationship for strip footings on sand with horizontal bedding and $F_0 = 0.4$ and $D_r = 30\%$

Fig. 11 (a) The incremental shear strain contour at s/B=0.25 and (b) the total shear strain contour at s/B=0.4. The sand has horizontal bedding and $D_r = 30\%$.

Fig. 12 Variation of Q_u for horizontal and vertical bedding at different D_r

Fig. 13 Mechanical response of Element A beneath the strip footings on sand with different density and bedding plane orientation

Fig. 14 Effect of density on the bearing capacity of strip footings on sand with horizontal bedding plane orientation: (a) $F_0 = 0$ and (b) $F_0 = 0.4$

Fig. 15 Effect of initial degree of anisotropy F_0 on the response of strip footings on sand with horizontal bedding plane orientation: (a) $D_r = 80\%$ and (b) $D_r = 50\%$

Fig. 16 Distribution of anisotropic variable A at s/B=0.11 for sand with $D_r = 80\%$ and (a) $F_0 = 0$, (b) $F_0 = 0.6$

Fig. 17 Comparison between the isotropic model prediction and drained triaxial compression test data on Toyour sand: (a) and (b) Dense sand; (c) and (d) Medium dense sand (data from data from Fukushima and Tatsuoka, 1984)

Fig. 18 Comparison between the isotropic model prediction and drained plane strain compression test data on Toyoura sand: (a) and (b) σ_3=200 kPa; (c) and (d) σ_3=50 kPa (data from Oda et al., 1978)

Fig. 19 Prediction of the isotropic model for the centrifuge tests on sand with horizontal bedding plane (data from Kimura et a., 1985)

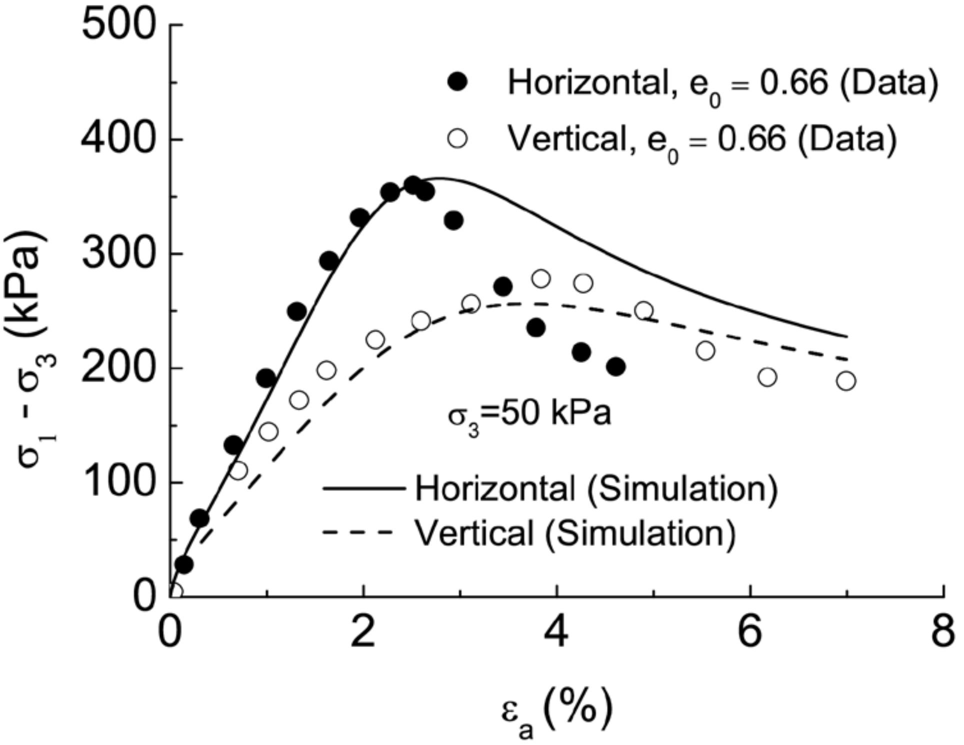
500
400
300
200
100
0
0
2
4
6
8
Horizontal, e_0 = 0.66 (Data)
Vertical, e_0 = 0.66 (Data)
$\sigma_1 - \sigma_3$ (kPa)
σ_3=50 kPa
Horizontal (Simulation)
Vertical (Simulation)
ε_a (%)

Fig. 1a

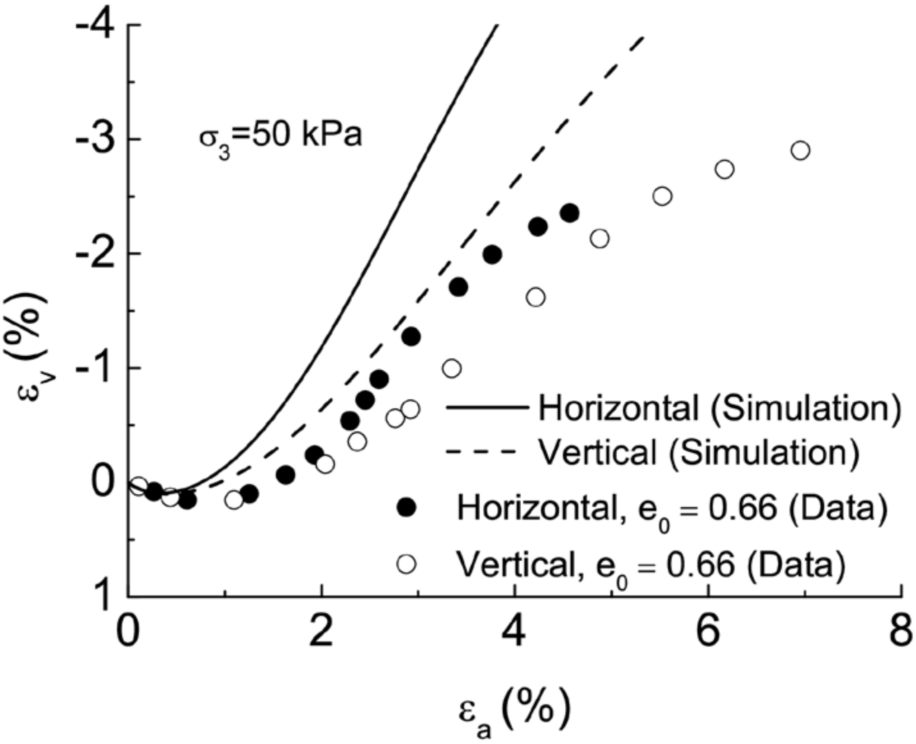
-4
-3
-2
-1
0
1
0
2
4
6
8
σ_3=50 kPa
ε_v (%)
Horizontal (Simulation)
Vertical (Simulation)
Horizontal, e_0 = 0.66 (Data)
Vertical, e_0 = 0.66 (Data)
ε_a (%)

Fig. 1b

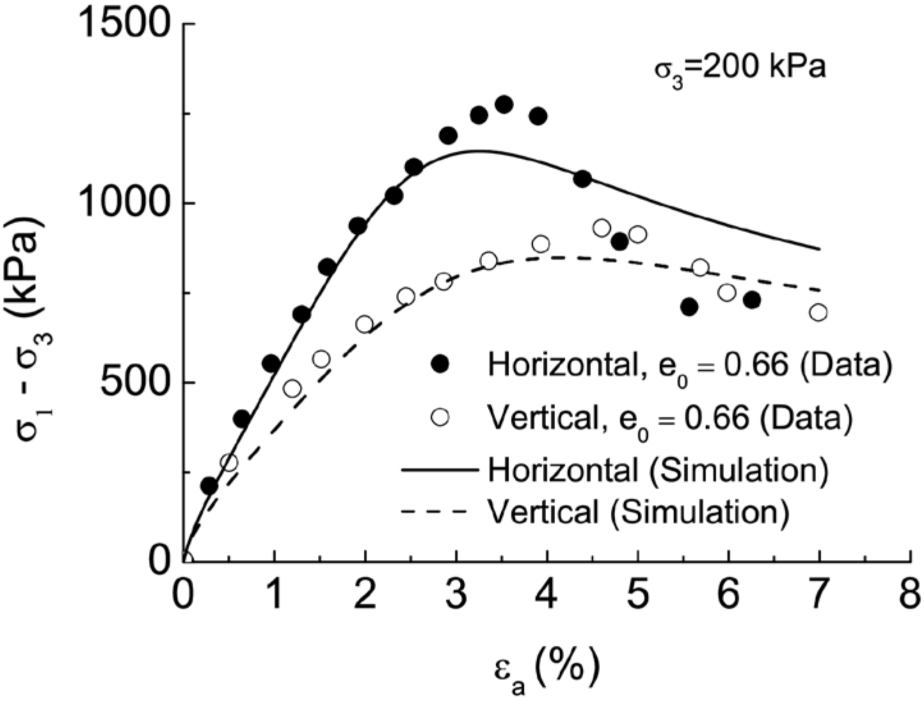

σ3=200 kPa
Horizontal, e0 = 0.66 (Data)
Vertical, e0 = 0.66 (Data)
Horizontal (Simulation)
Vertical (Simulation)
σ1 - σ3 (kPa)
εa (%)

Fig. 1c

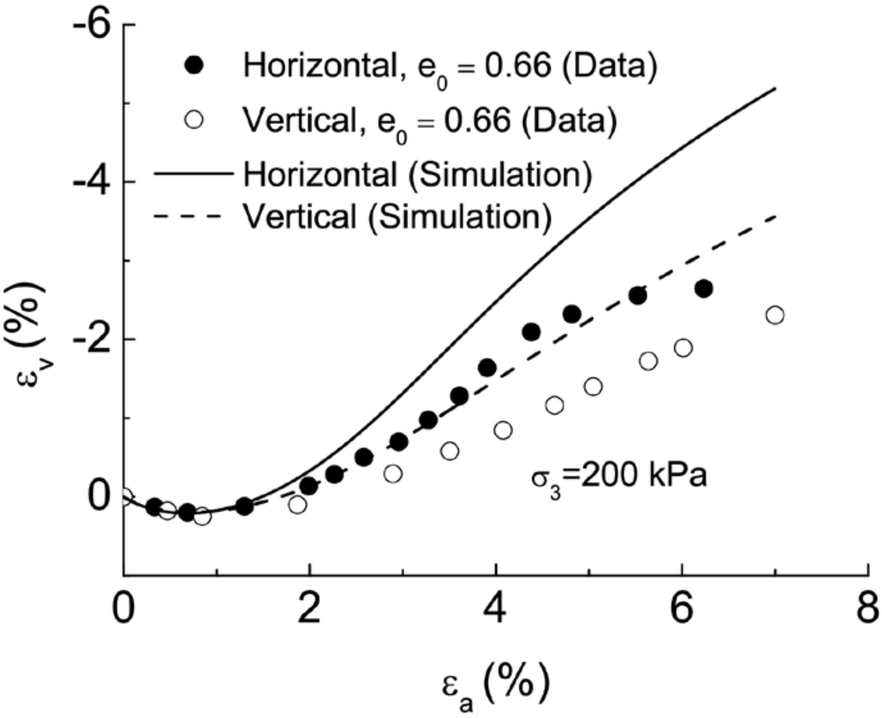

Horizontal, e0 = 0.66 (Data)
Vertical, e0 = 0.66 (Data)
Horizontal (Simulation)
Vertical (Simulation)
σ3=200 kPa
εv (%)
εa (%)

Fig. 1d

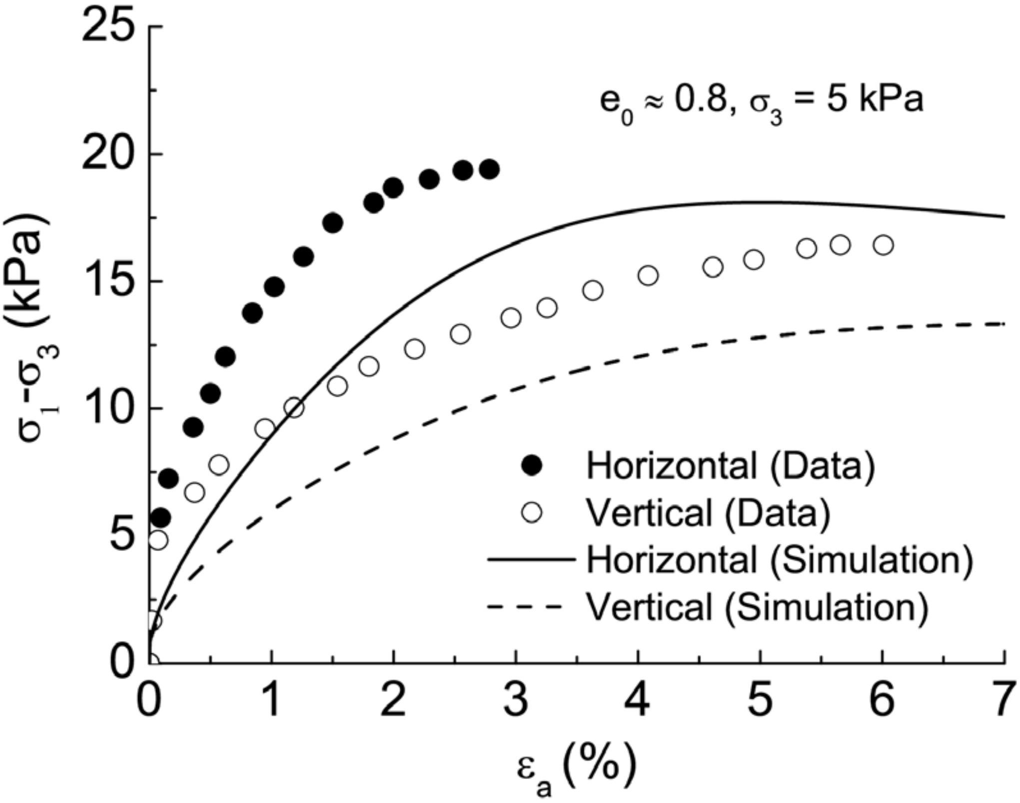
e0 ≈ 0.8, σ3 = 5 kPa
Horizontal (Data)
Vertical (Data)
Horizontal (Simulation)
Vertical (Simulation)
σ1-σ3 (kPa)
εa (%)
0
5
10
15
20
25
0
1
2
3
4
5
6
7

Fig. 2a

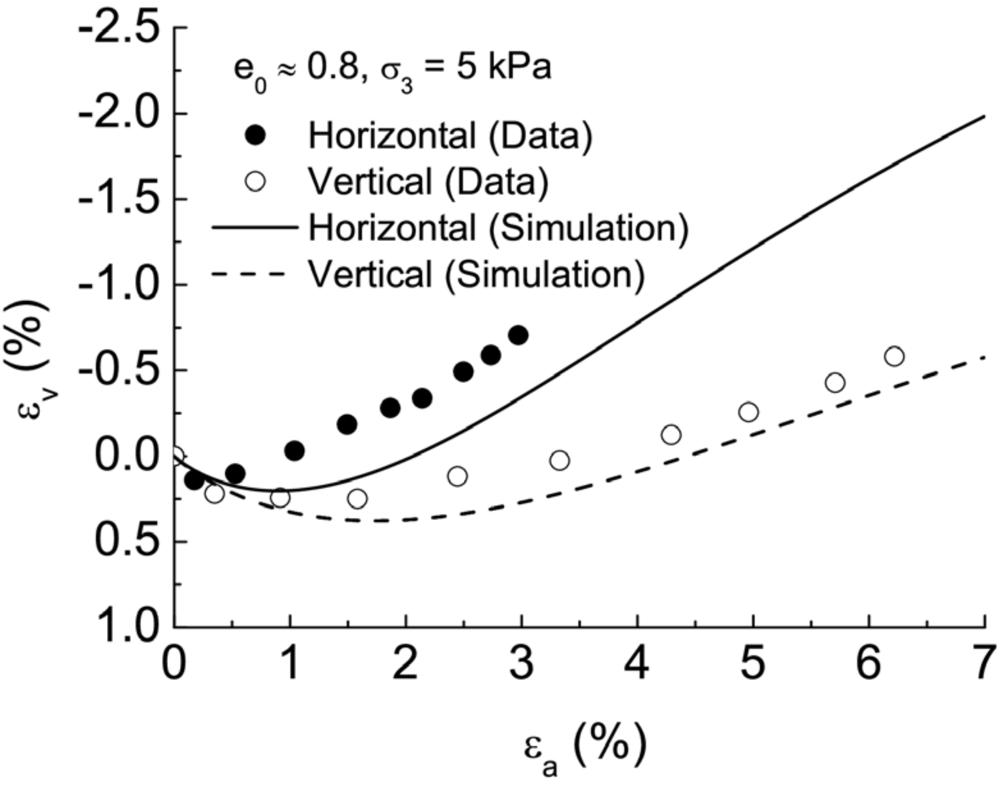
e0 ≈ 0.8, σ3 = 5 kPa
Horizontal (Data)
Vertical (Data)
Horizontal (Simulation)
Vertical (Simulation)
εv (%)
εa (%)
-2.5
-2.0
-1.5
-1.0
-0.5
0.0
0.5
1.0
0
1
2
3
4
5
6
7

Fig. 2b

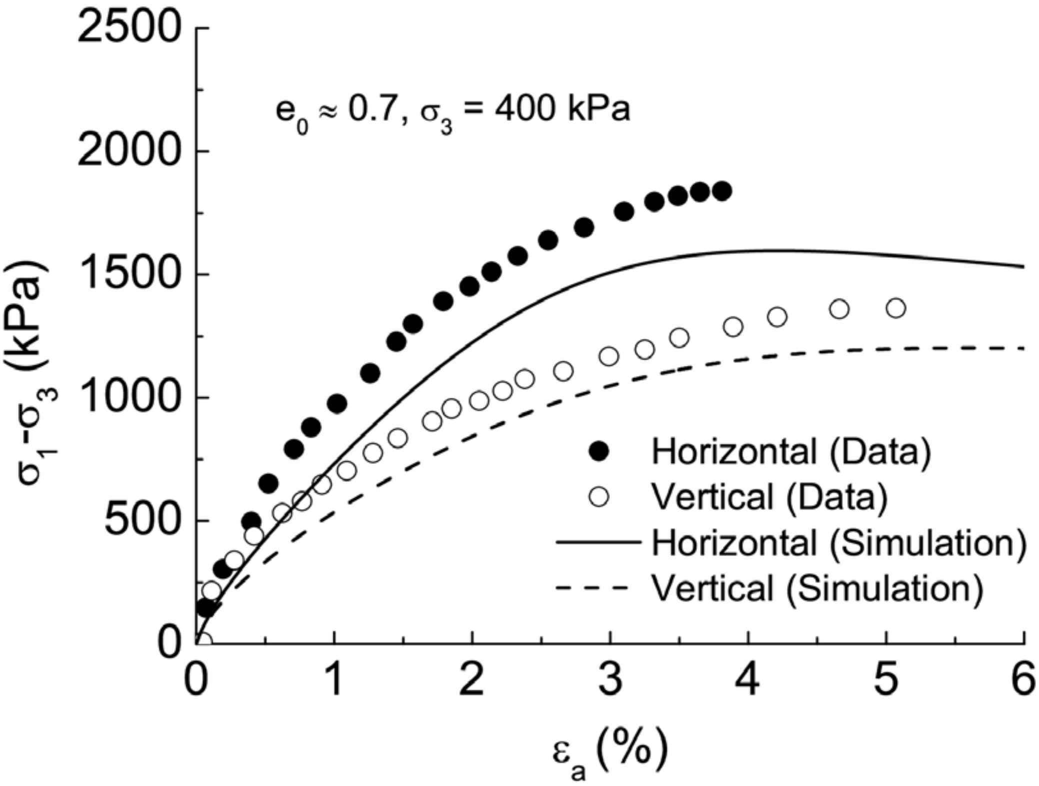

2500
2000
1500
1000
500
0
σ1-σ3 (kPa)
e0 ≈ 0.7, σ3 = 400 kPa
Horizontal (Data)
Vertical (Data)
Horizontal (Simulation)
Vertical (Simulation)
0 1 2 3 4 5 6
εa (%)

Fig. 2c

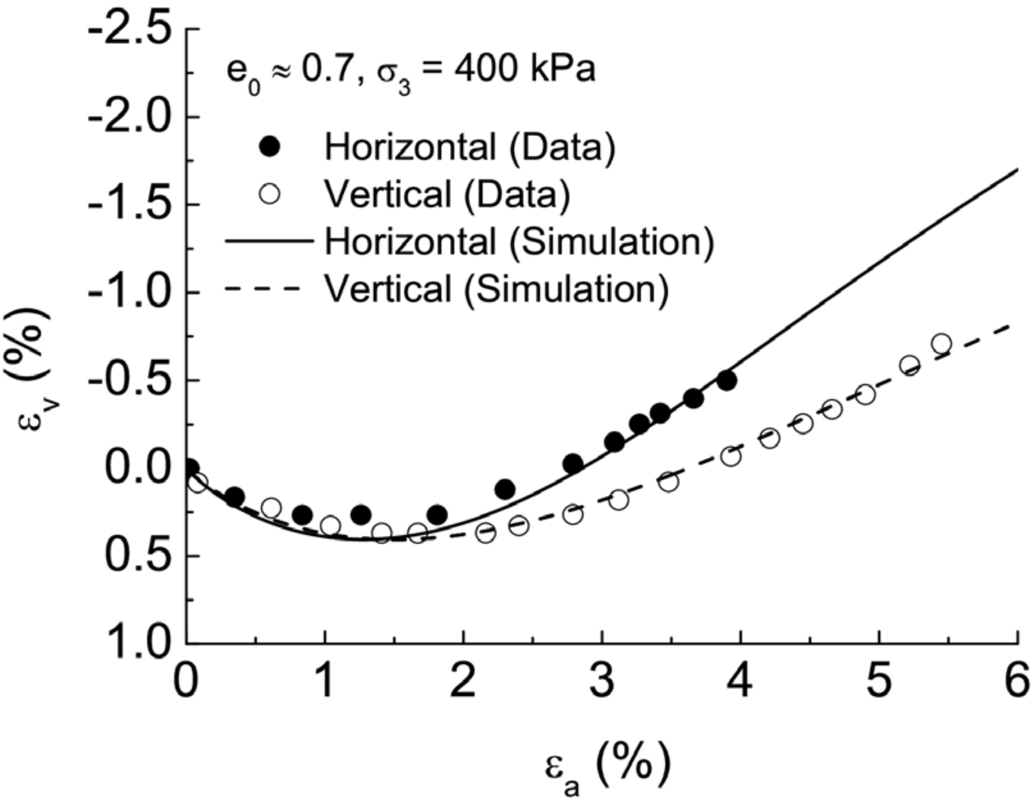

-2.5
-2.0
-1.5
-1.0
-0.5
0.0
0.5
1.0
εv (%)
e0 ≈ 0.7, σ3 = 400 kPa
Horizontal (Data)
Vertical (Data)
Horizontal (Simulation)
Vertical (Simulation)
0 1 2 3 4 5 6
εa (%)

Fig. 2d

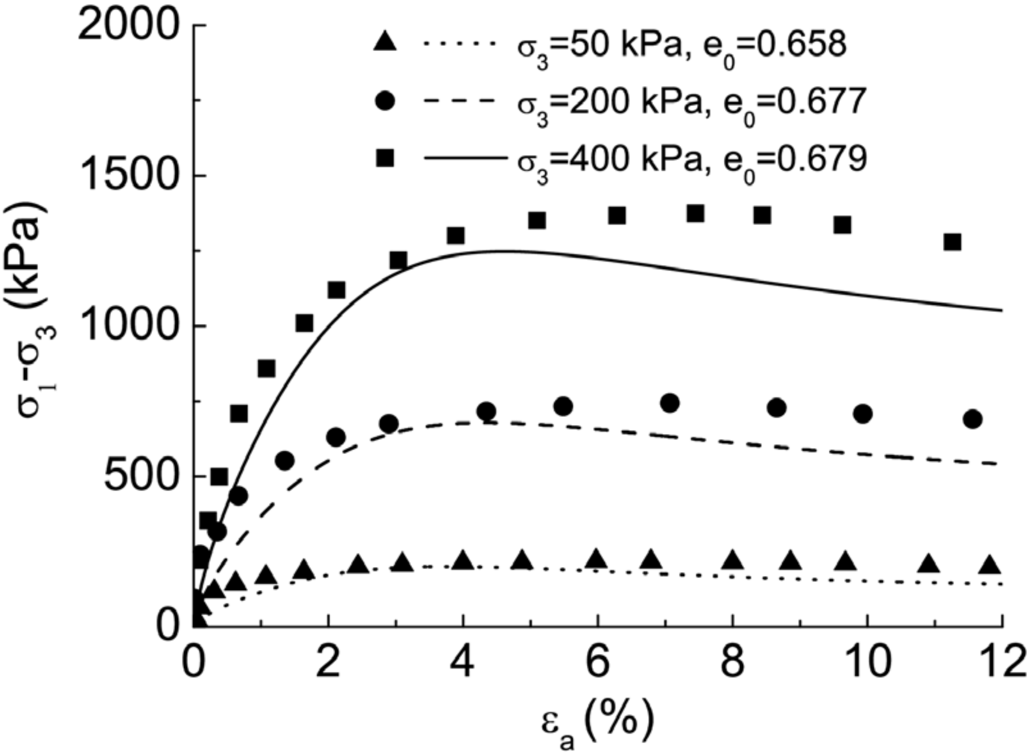
σ_3=50 kPa, e_0=0.658
σ_3=200 kPa, e_0=0.677
σ_3=400 kPa, e_0=0.679
σ_1-σ_3 (kPa)
ε_a (%)
0
500
1000
1500
2000
0
2
4
6
8
10
12

Fig. 3a

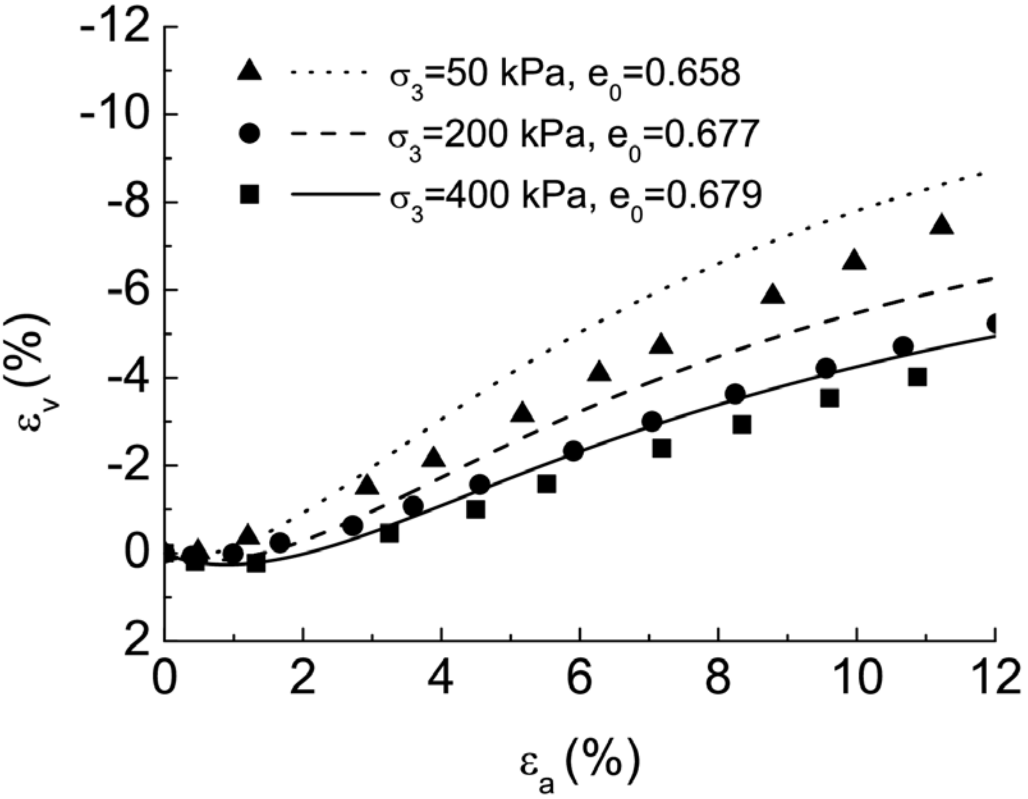
σ_3=50 kPa, e_0=0.658
σ_3=200 kPa, e_0=0.677
σ_3=400 kPa, e_0=0.679
ε_v (%)
ε_a (%)
-12
-10
-8
-6
-4
-2
0
2
0
2
4
6
8
10
12

Fig. 3b

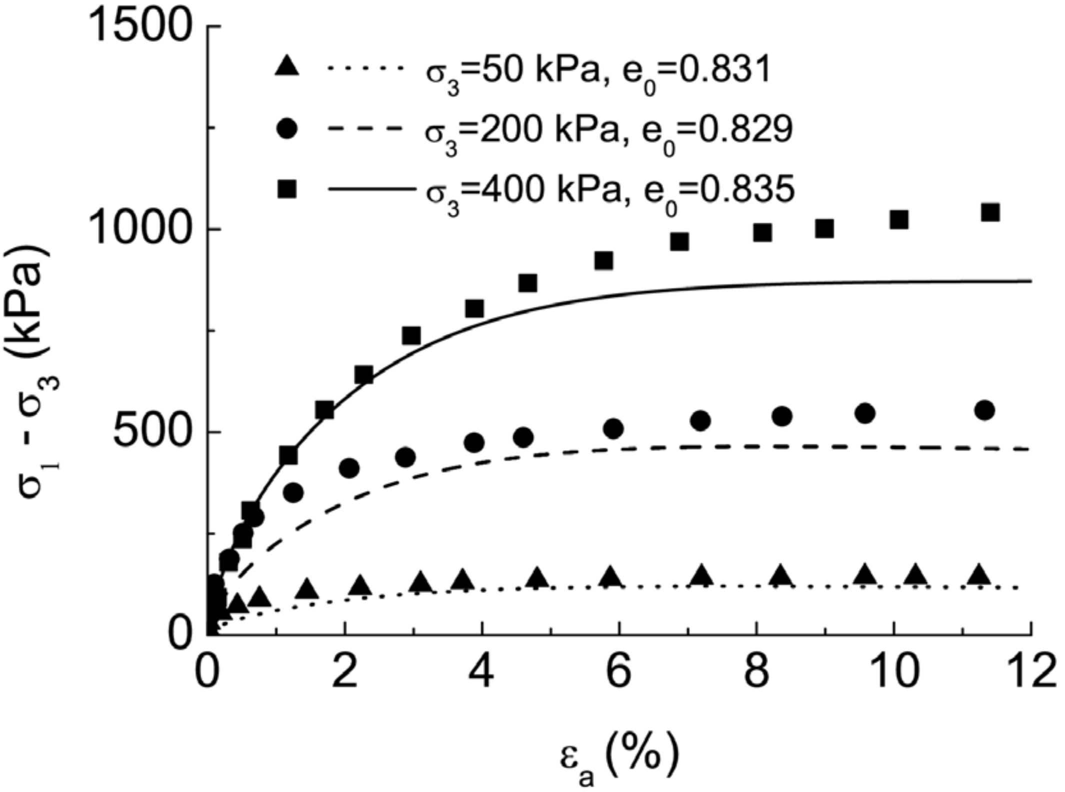

σ_3=50 kPa, e_0=0.831
σ_3=200 kPa, e_0=0.829
σ_3=400 kPa, e_0=0.835
$\sigma_1 - \sigma_3$ (kPa)
1500
1000
500
0
0
2
4
6
8
10
12
ε_a (%)

Fig. 3c

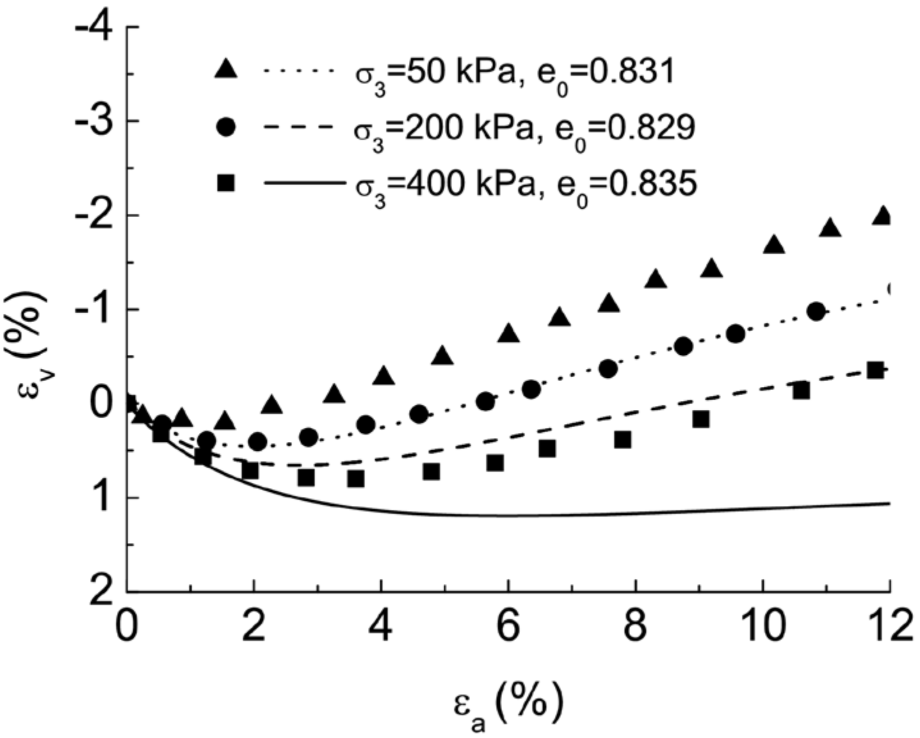

σ_3=50 kPa, e_0=0.831
σ_3=200 kPa, e_0=0.829
σ_3=400 kPa, e_0=0.835
ε_v (%)
-4
-3
-2
-1
0
1
2
0
2
4
6
8
10
12
ε_a (%)

Fig. 3d

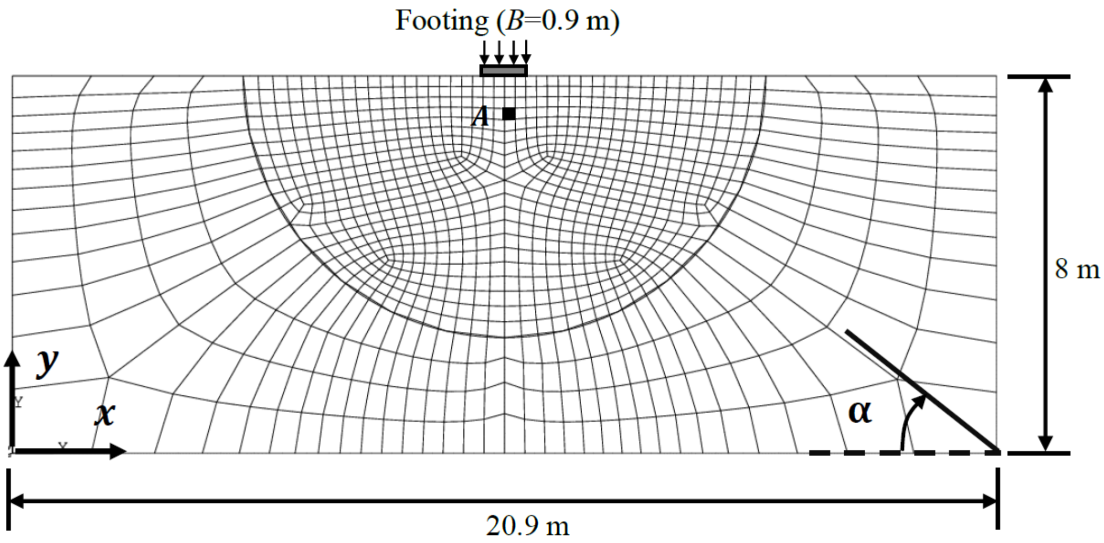
Footing (B=0.9 m)
A
y
x
α
8 m
20.9 m

Fig.4

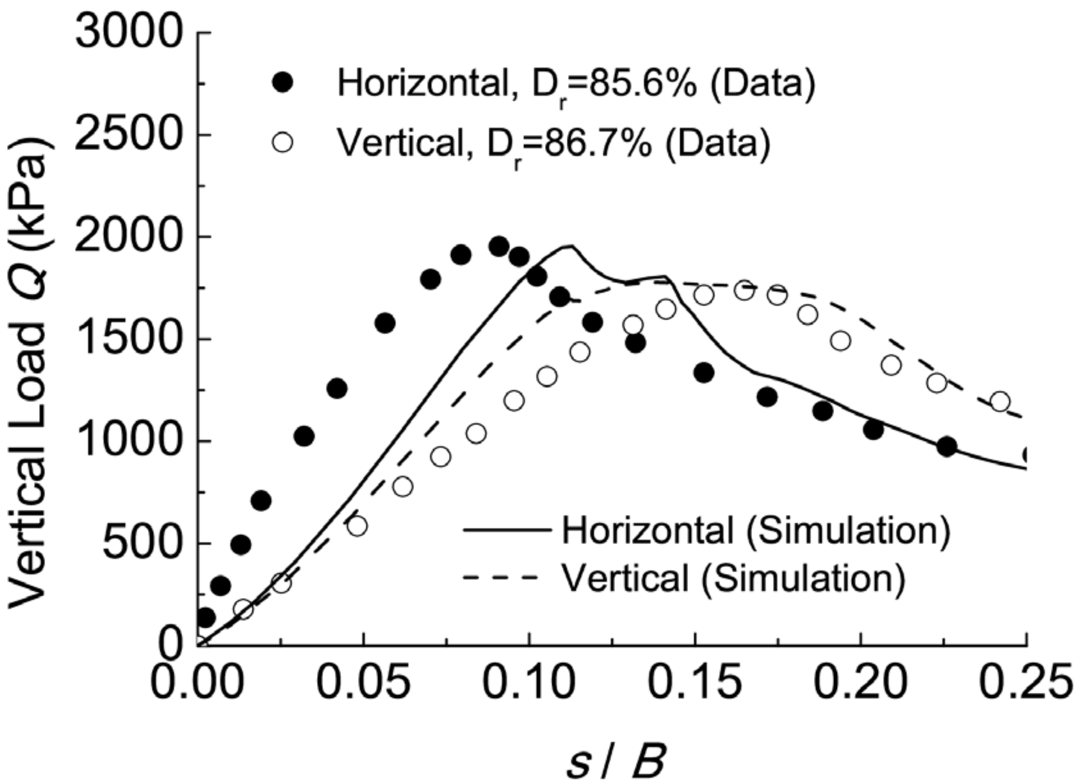
Horizontal, Dr=85.6% (Data)
Vertical, Dr=86.7% (Data)
Horizontal (Simulation)
Vertical (Simulation)
Vertical Load Q (kPa)
s / B
0
500
1000
1500
2000
2500
3000
0.00
0.05
0.10
0.15
0.20
0.25

Fig. 5a

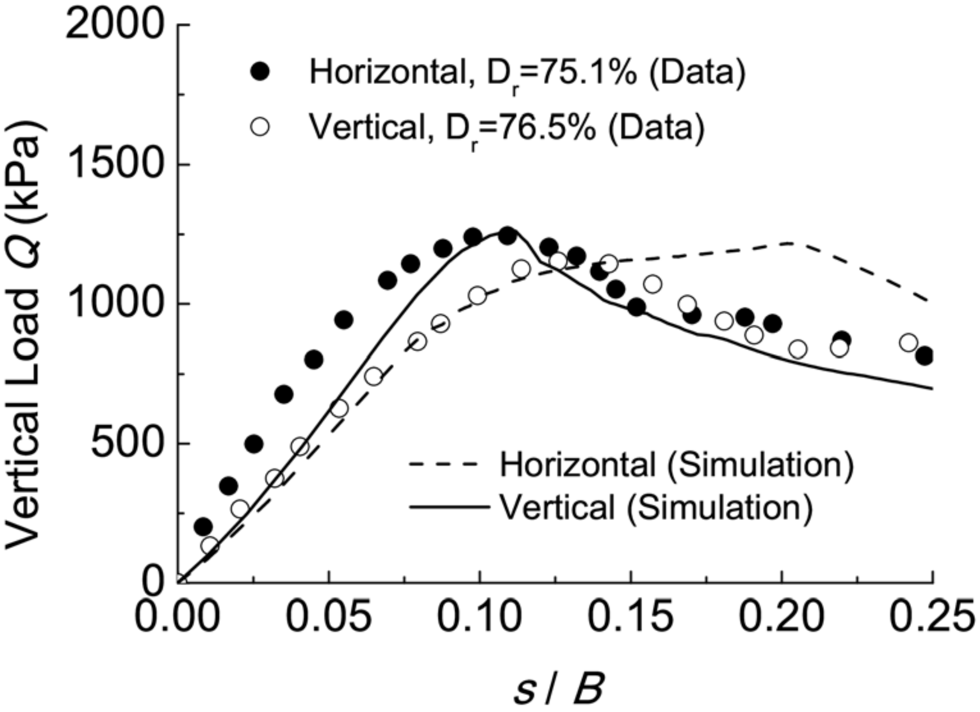
Horizontal, D_r=75.1% (Data)
Vertical, D_r=76.5% (Data)
Horizontal (Simulation)
Vertical (Simulation)
Vertical Load Q (kPa)
s / B
0
500
1000
1500
2000
0.00
0.05
0.10
0.15
0.20
0.25

Fig. 5b

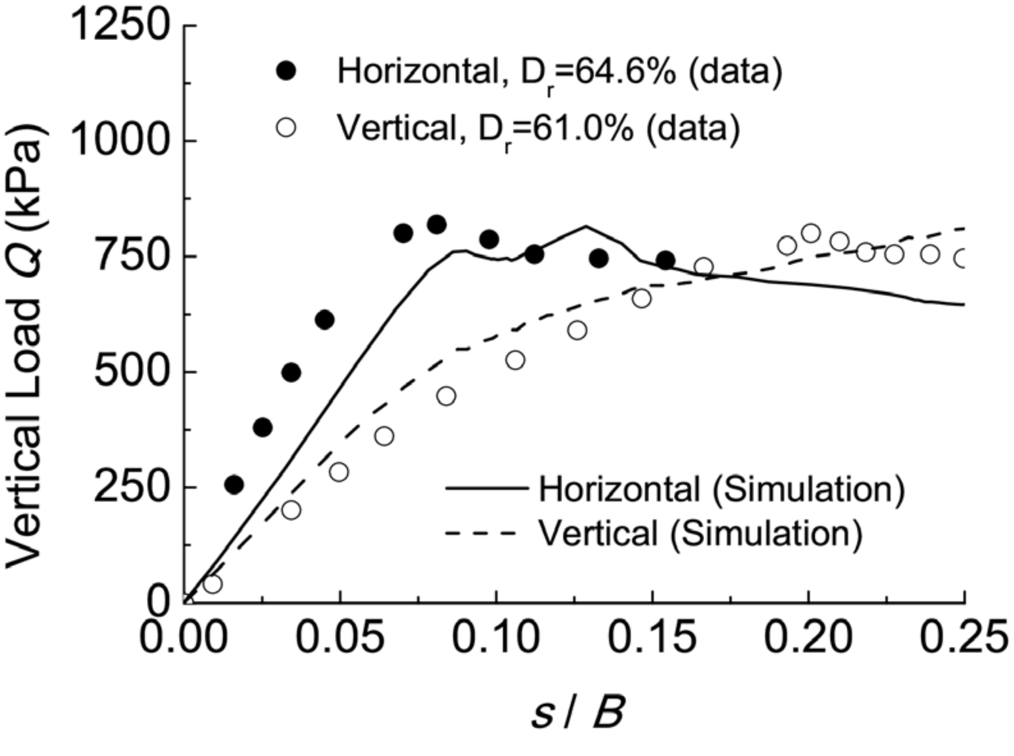
Horizontal, D_r=64.6% (data)
Vertical, D_r=61.0% (data)
Horizontal (Simulation)
Vertical (Simulation)
Vertical Load Q (kPa)
s / B
0
250
500
750
1000
1250
0.00
0.05
0.10
0.15
0.20
0.25

Fig. 5c

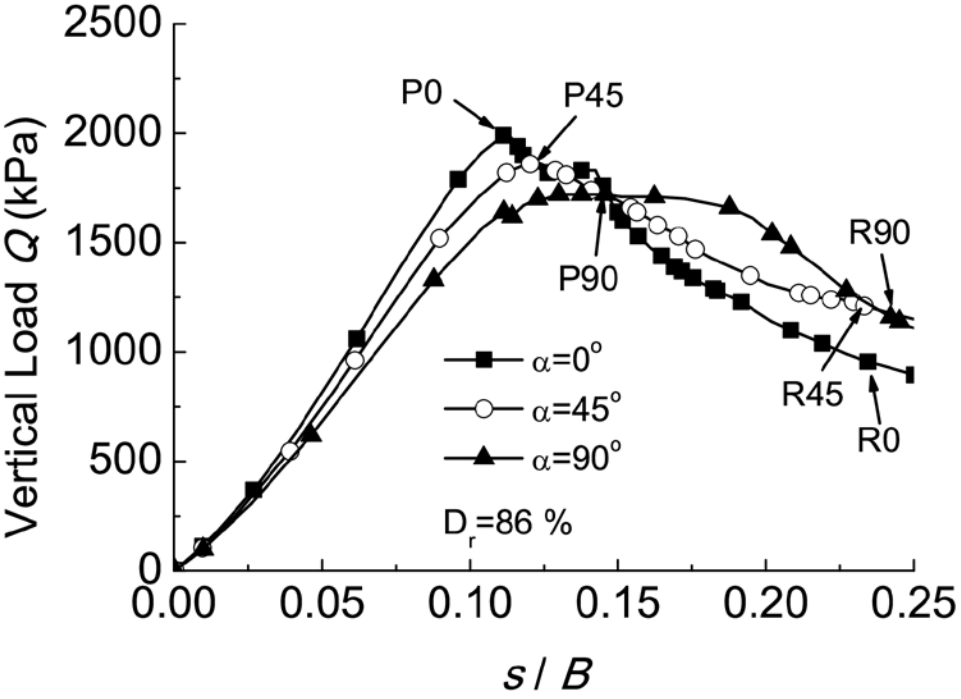

2500
2000
1500
1000
500
0
0.00
0.05
0.10
0.15
0.20
0.25
Vertical Load Q (kPa)
s / B
P0
P45
P90
R90
R45
R0
α=0°
α=45°
α=90°
Dr=86 %

Fig. 6a

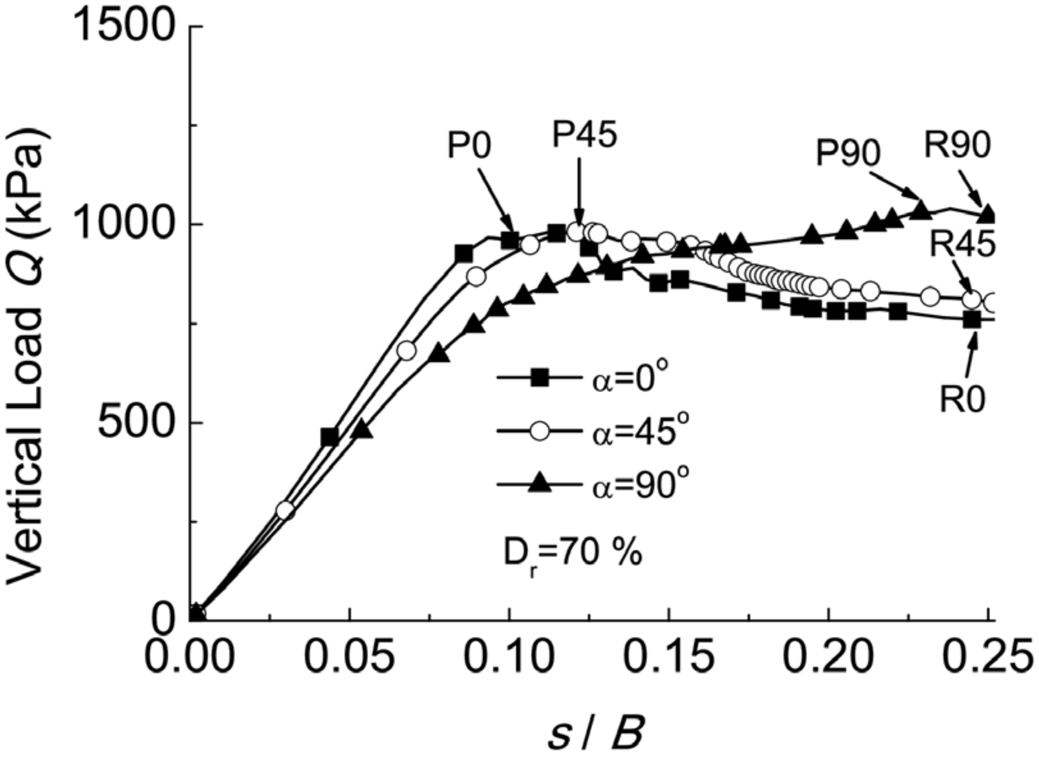

1500
1000
500
0
0.00
0.05
0.10
0.15
0.20
0.25
Vertical Load Q (kPa)
s / B
P0
P45
P90
R90
R45
R0
α=0°
α=45°
α=90°
Dr=70 %

Fig. 6b

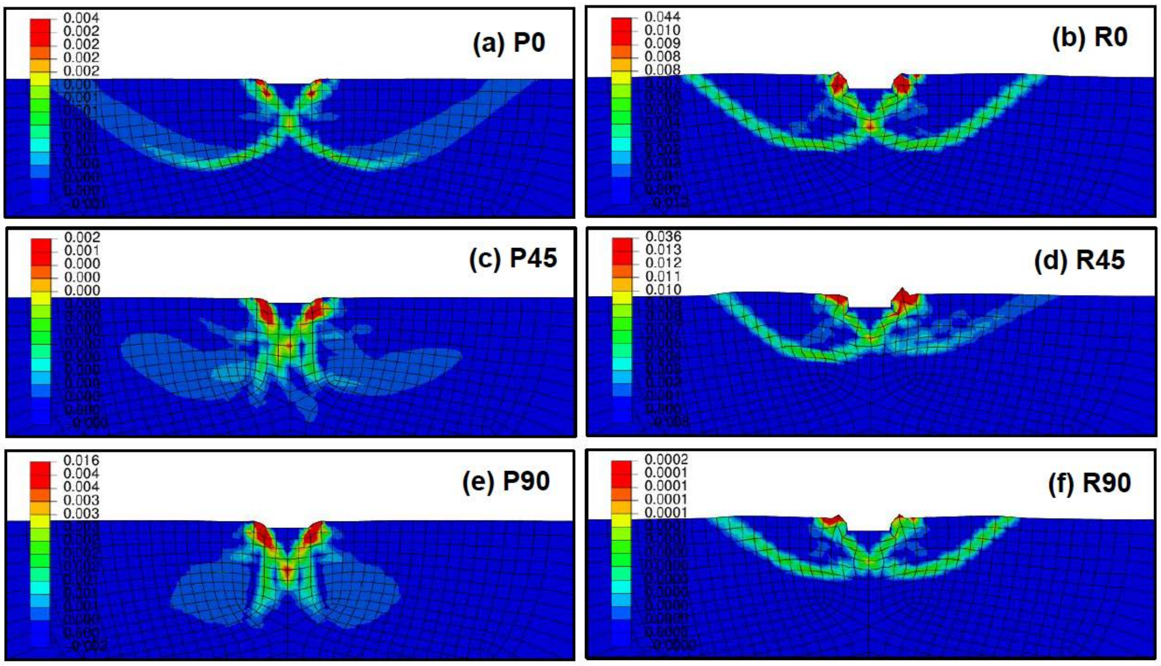

Fig. 7

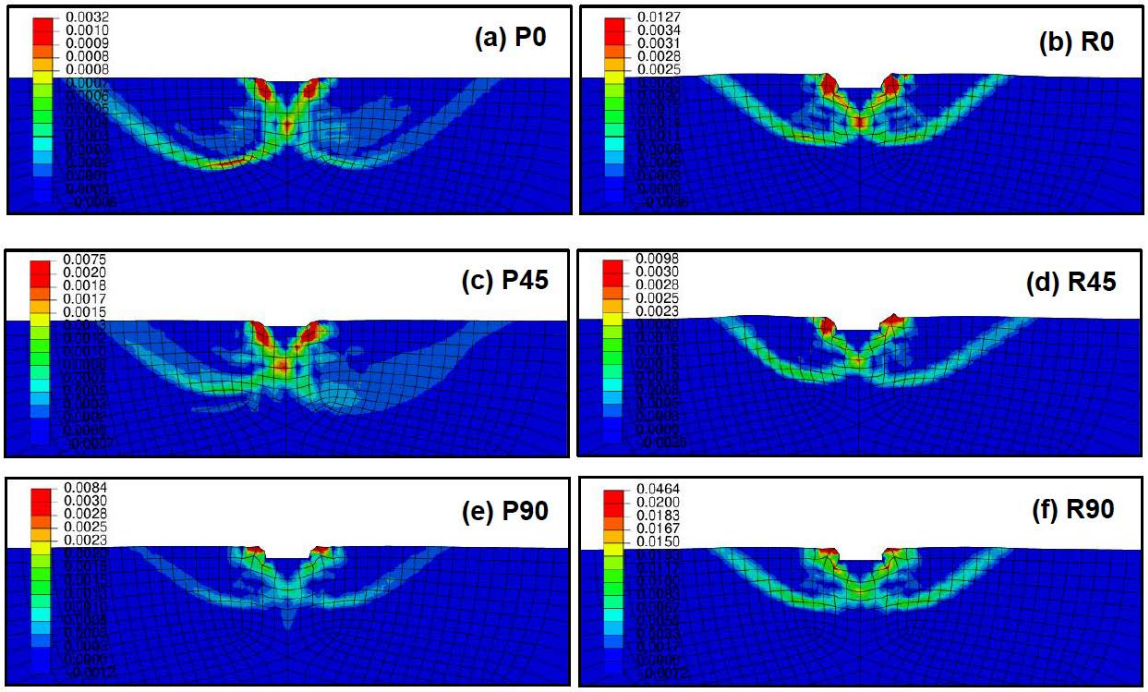

Fig. 8

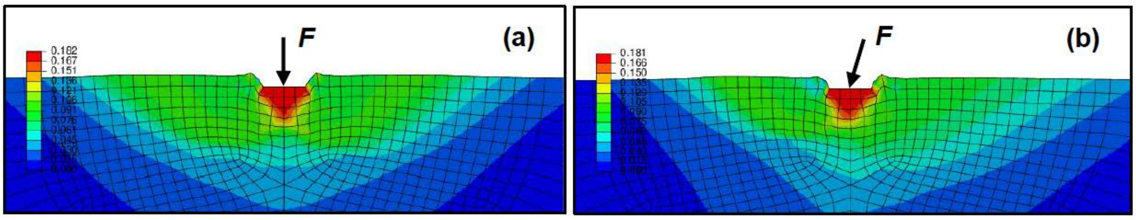

Fig. 9

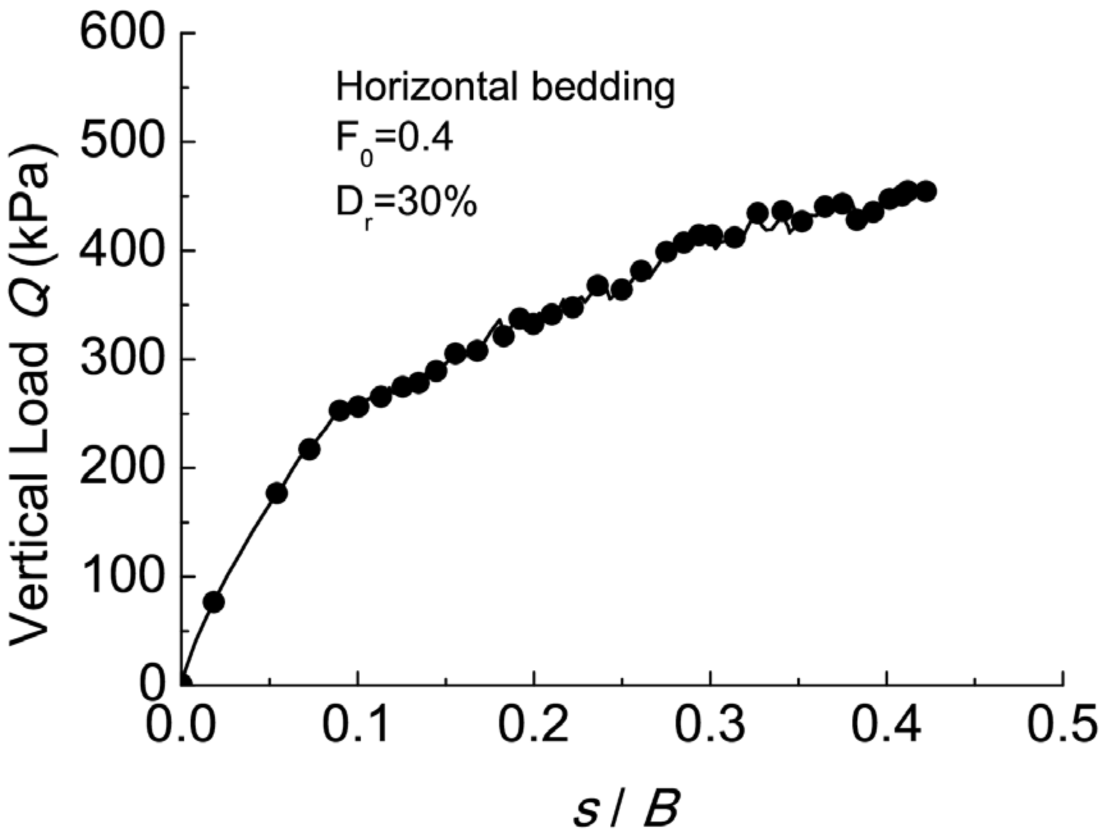

Fig. 10

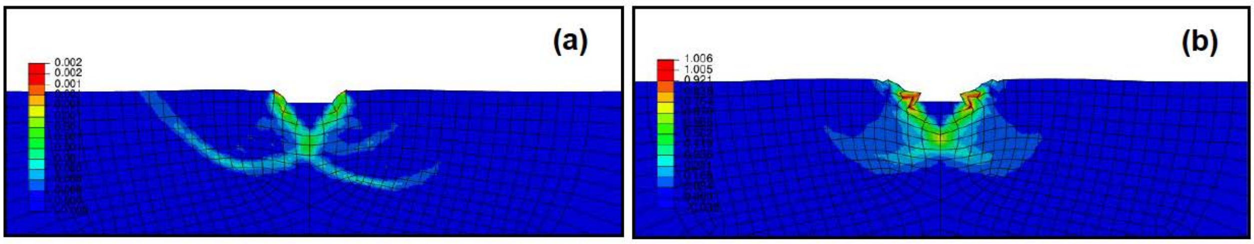

Fig. 11

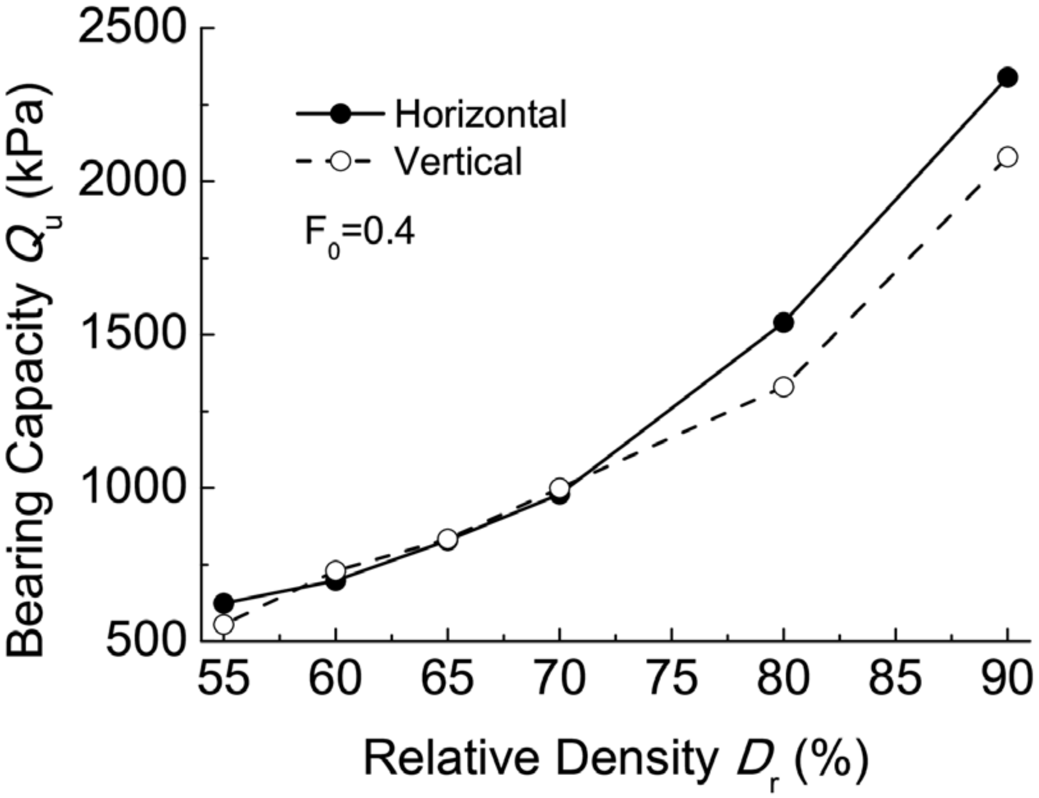

Fig. 12

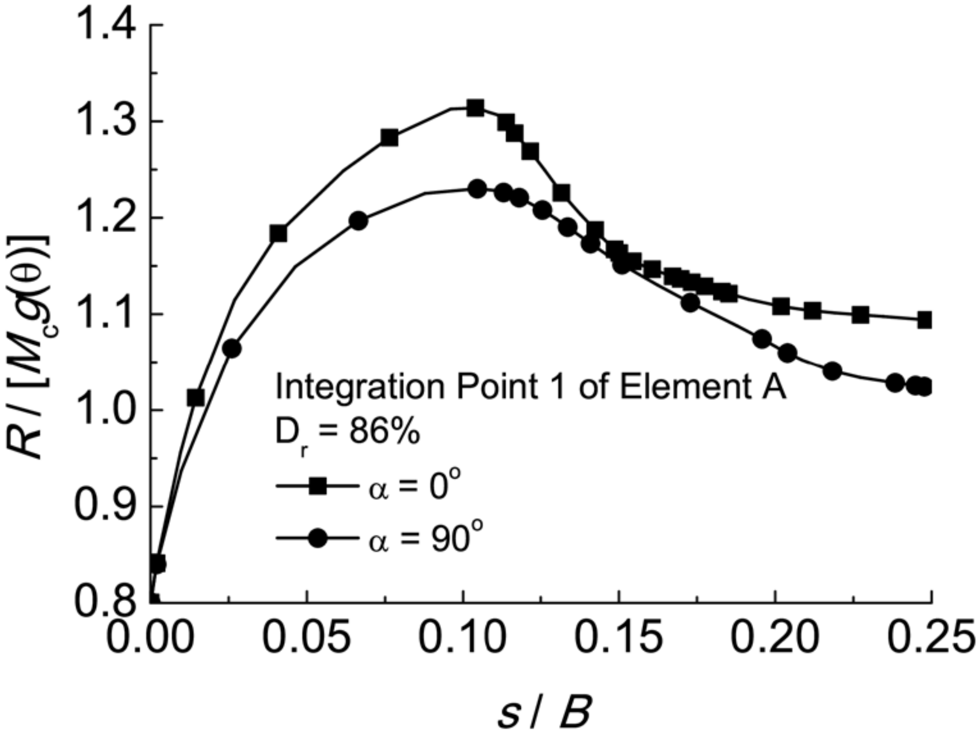

Fig. 13a

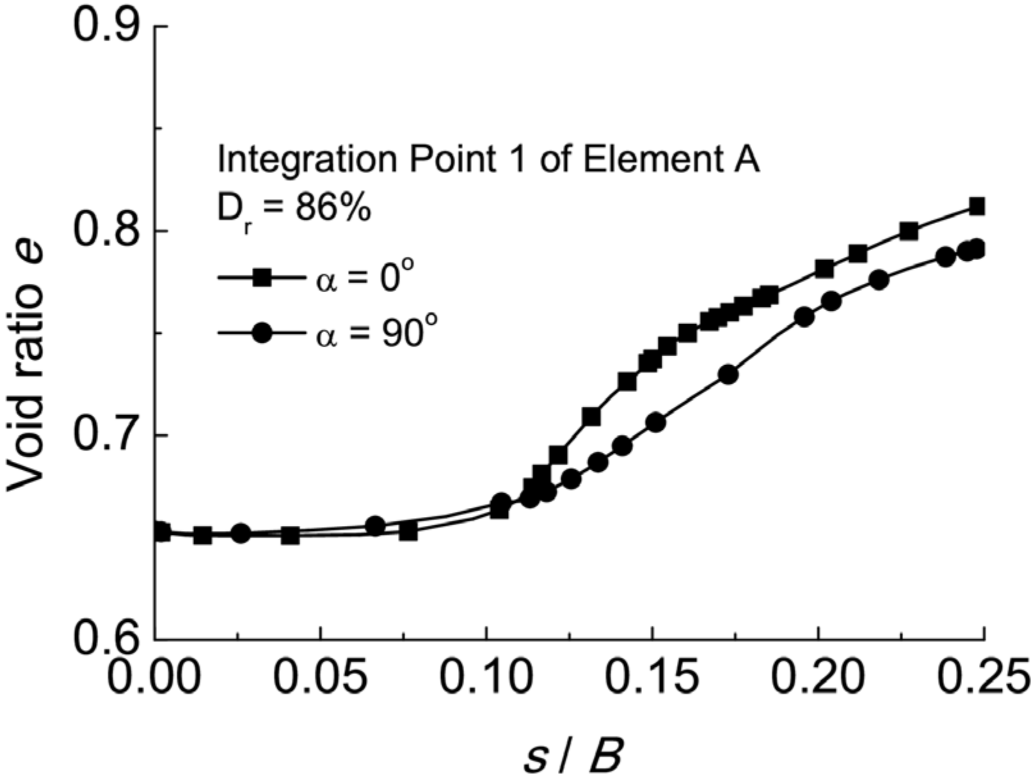

Fig. 13b

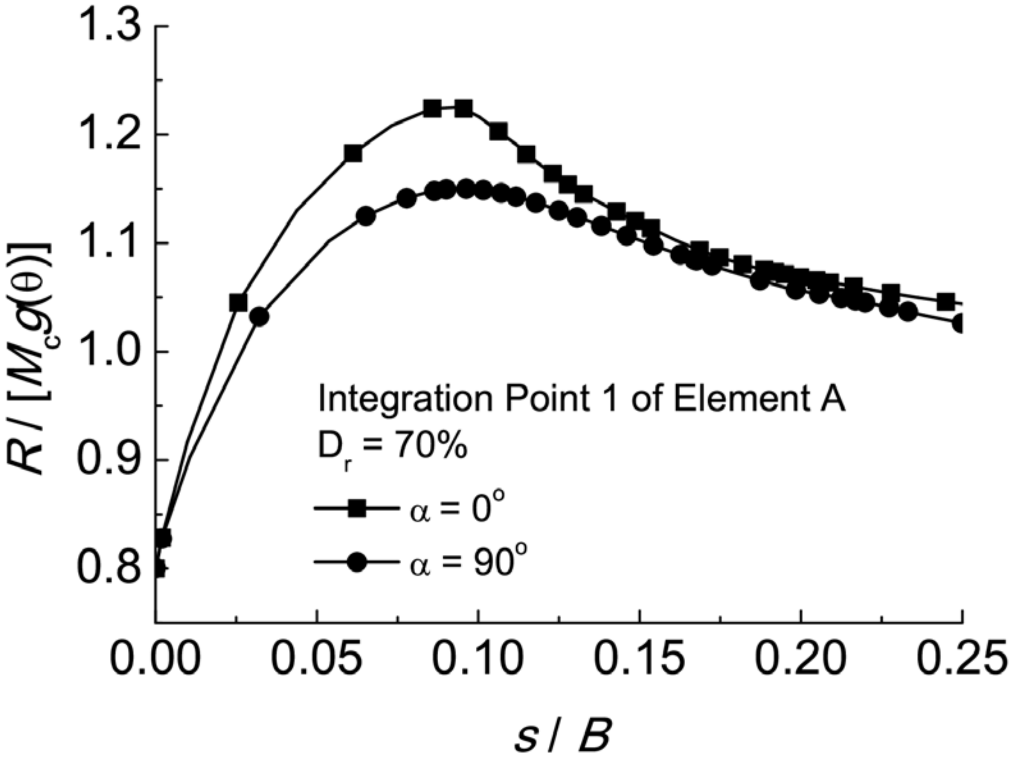

Fig. 13c

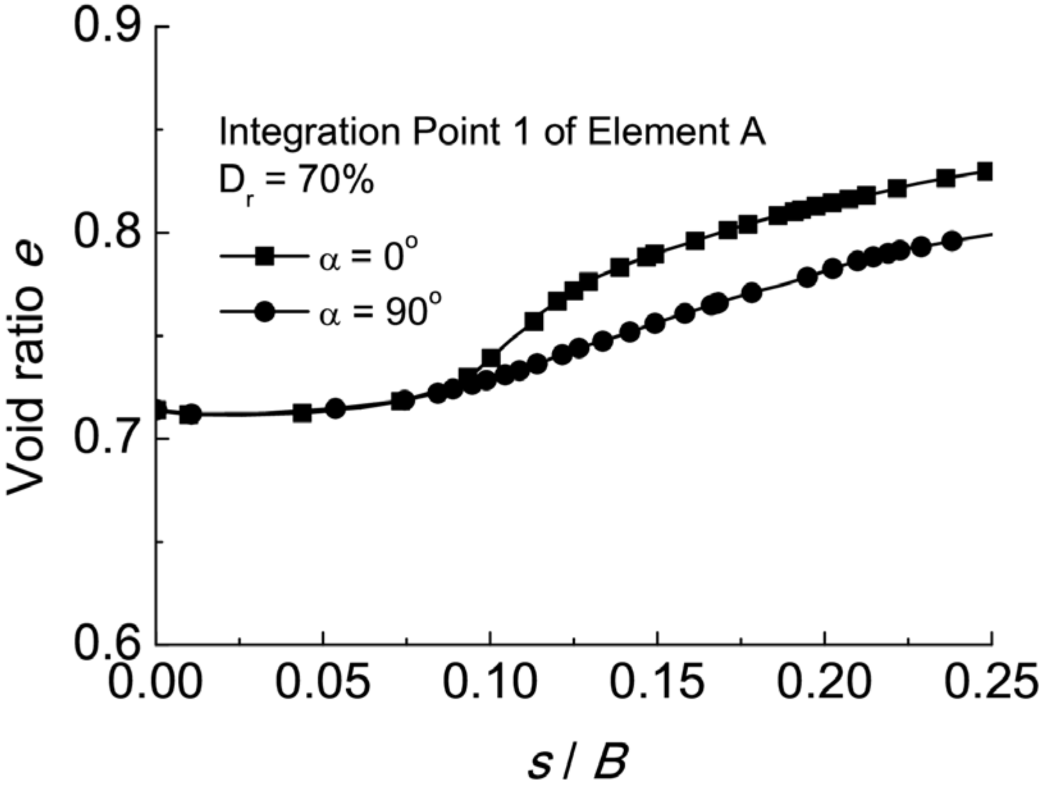

Fig. 13d

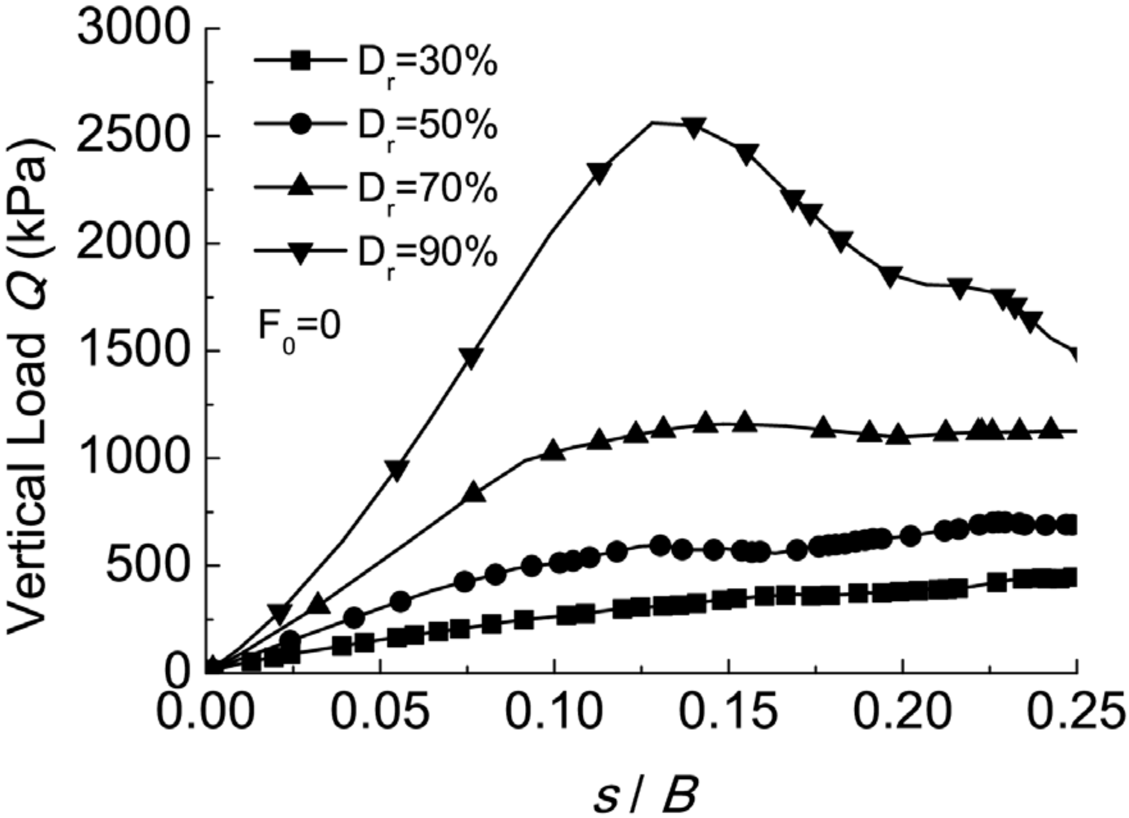

Fig. 14a

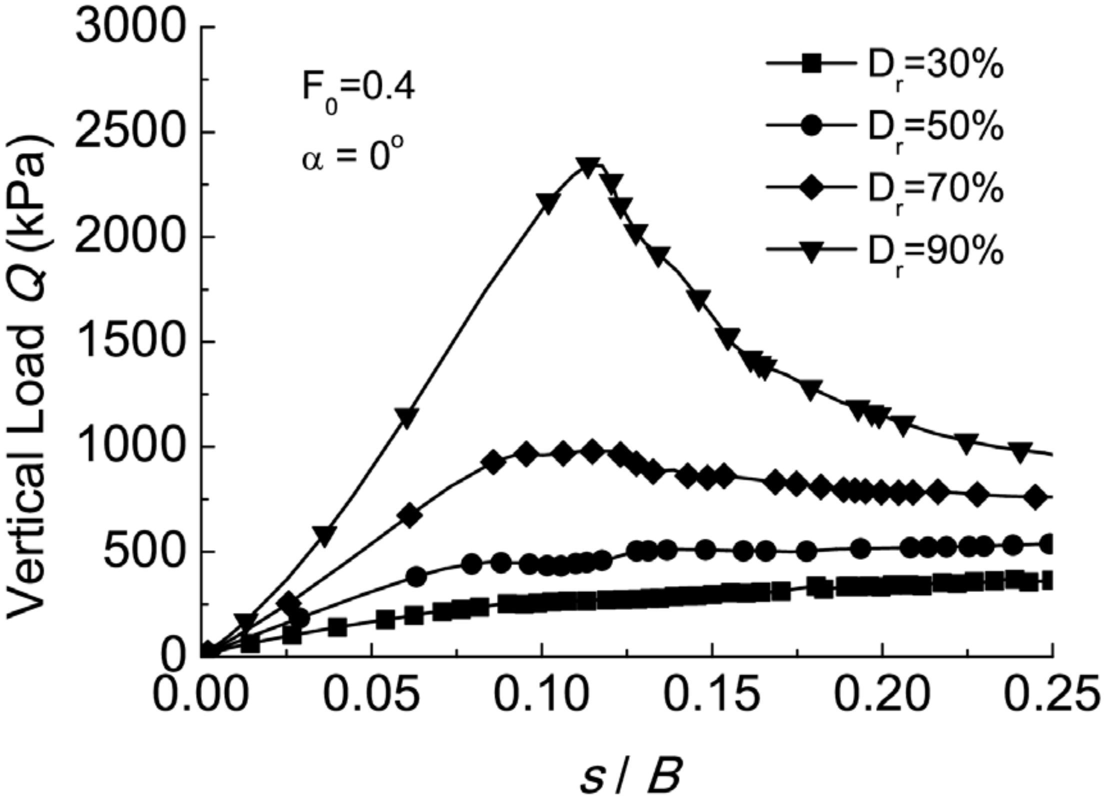

Fig. 14b

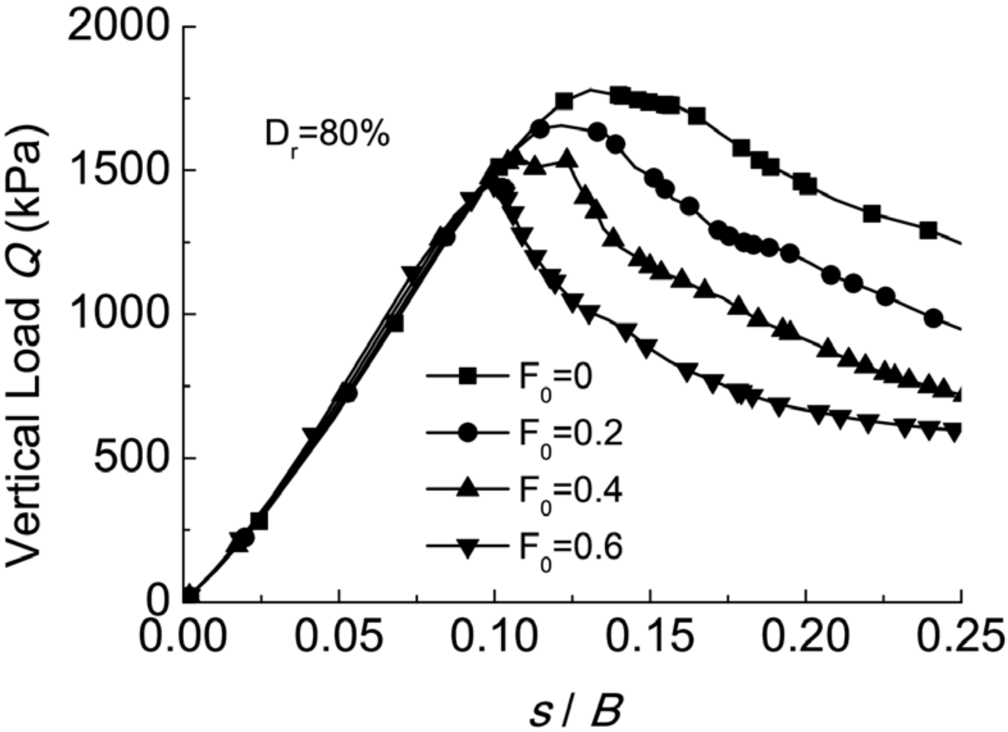

Fig. 15a

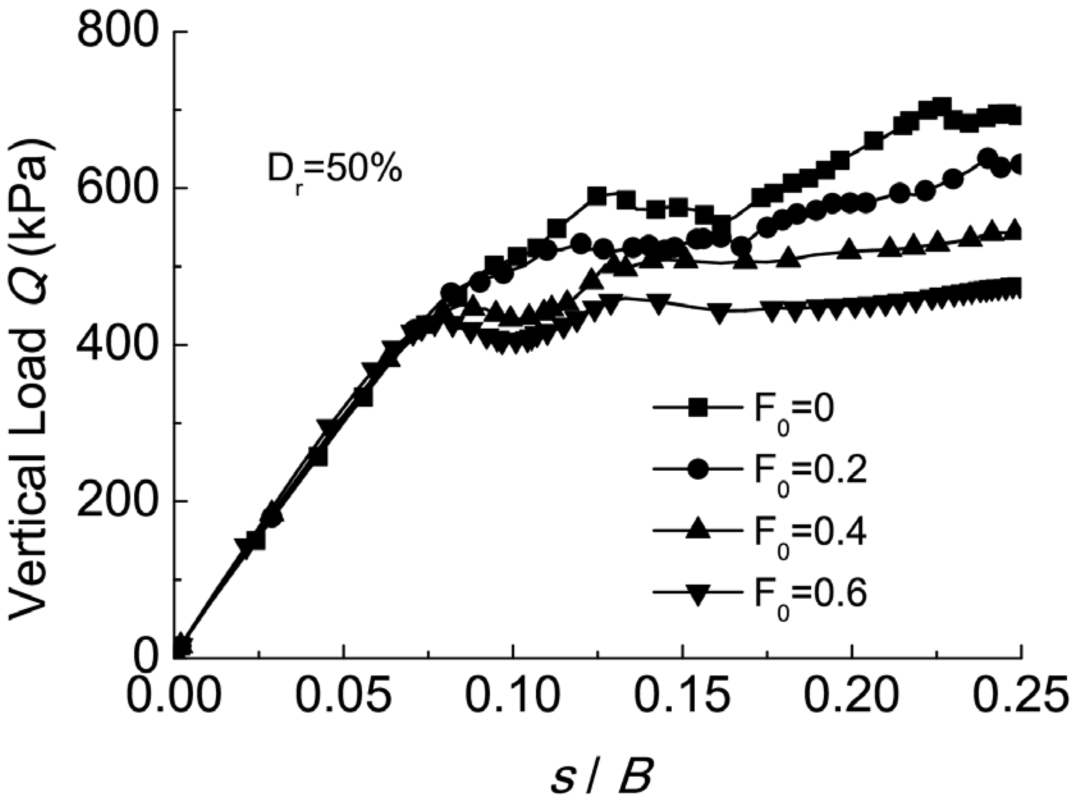

Fig. 15b

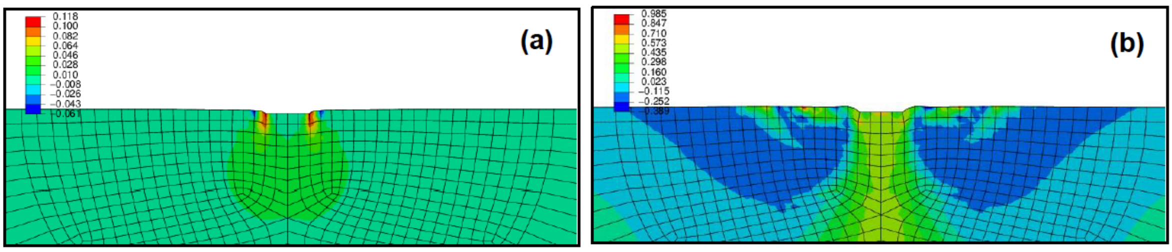

Fig. 16

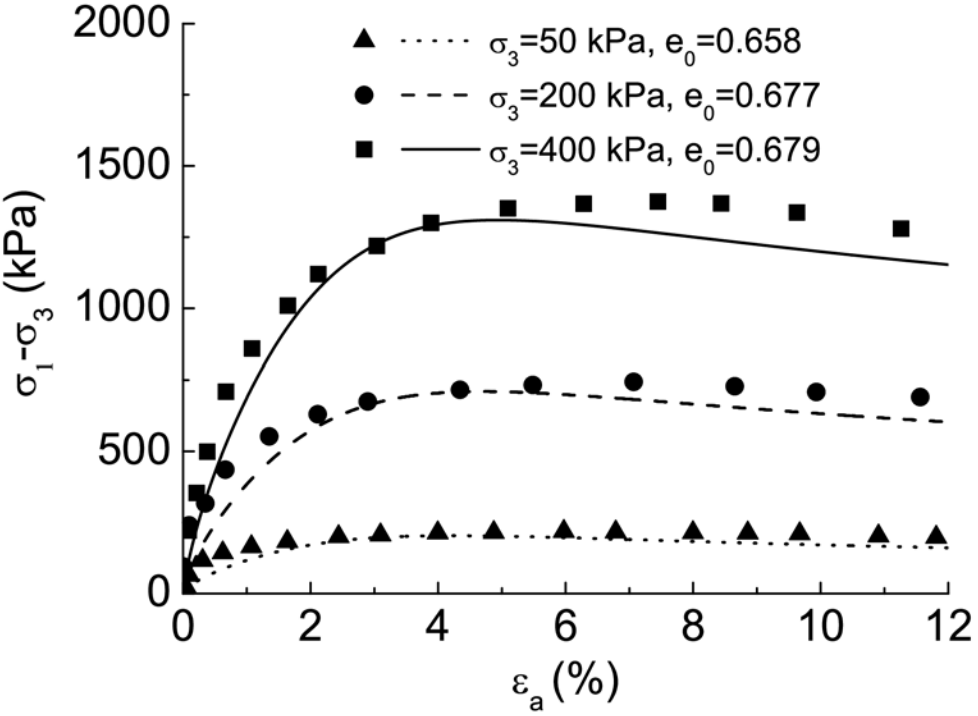

Fig. 17a

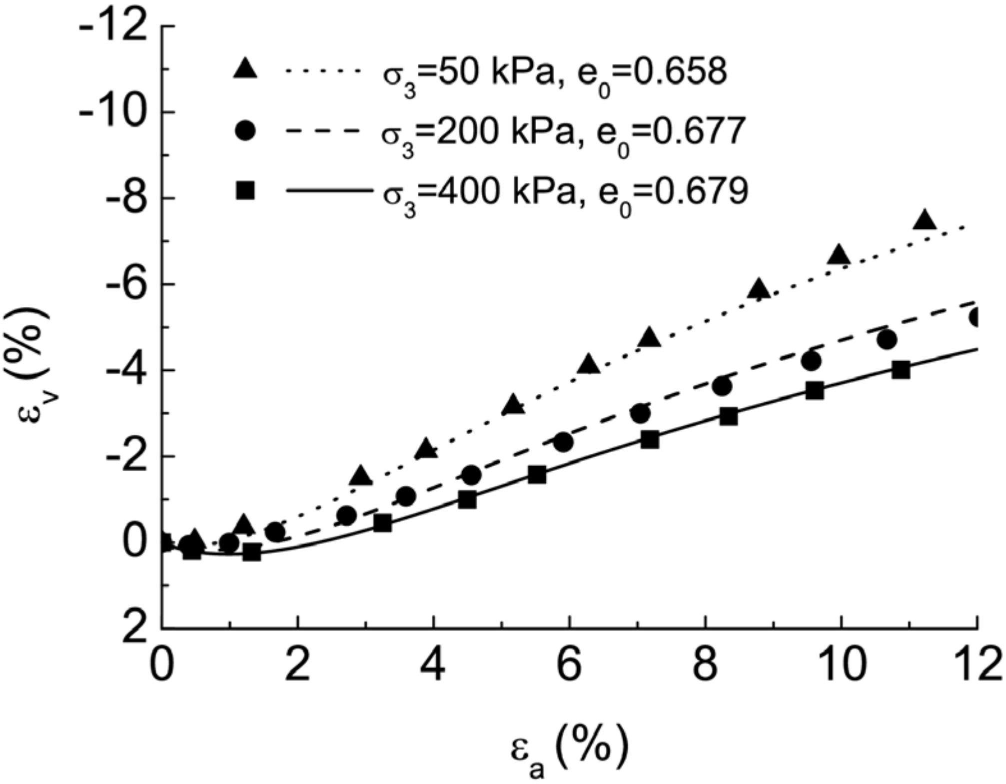

Fig. 17b

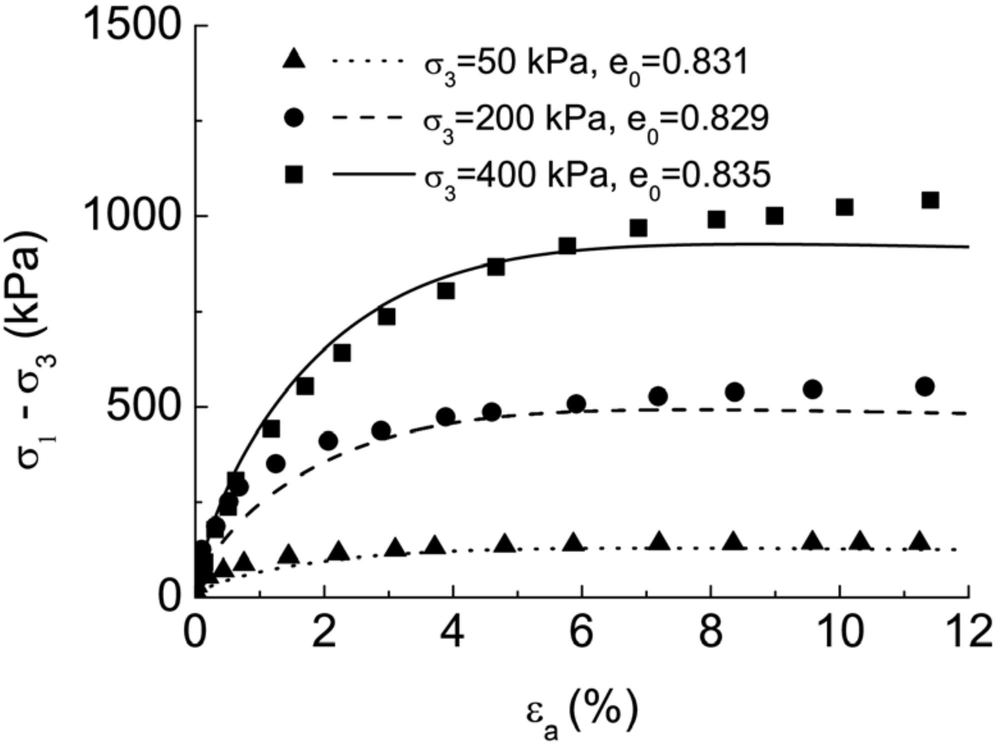

Fig. 17c

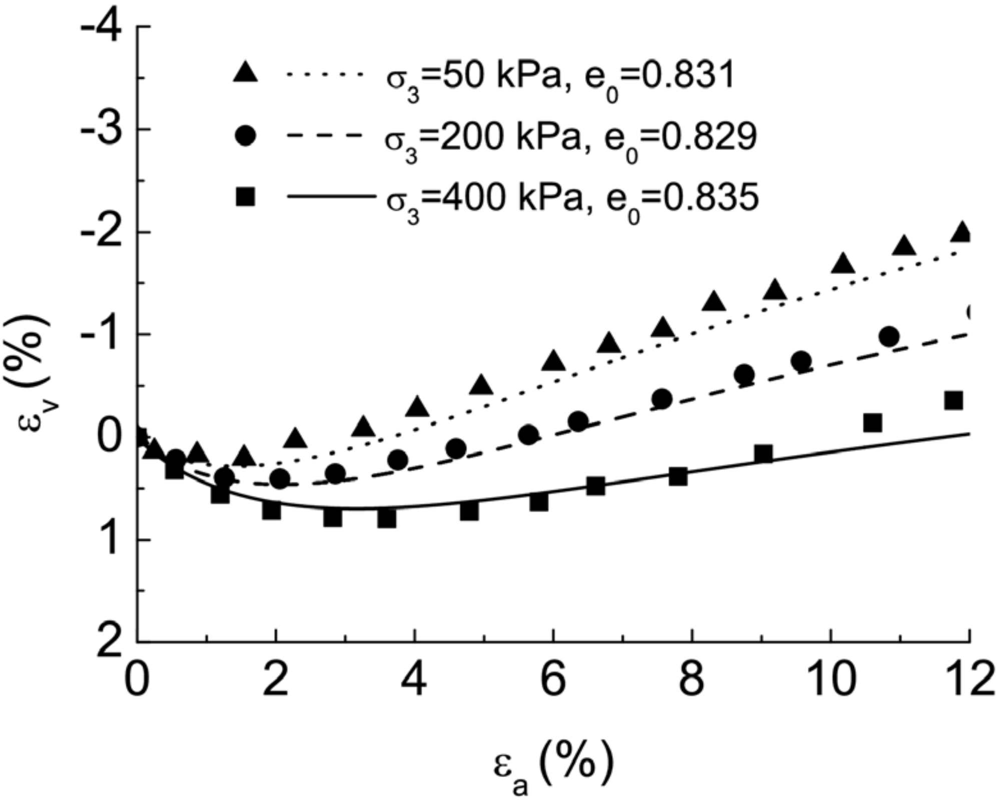

Fig. 17d

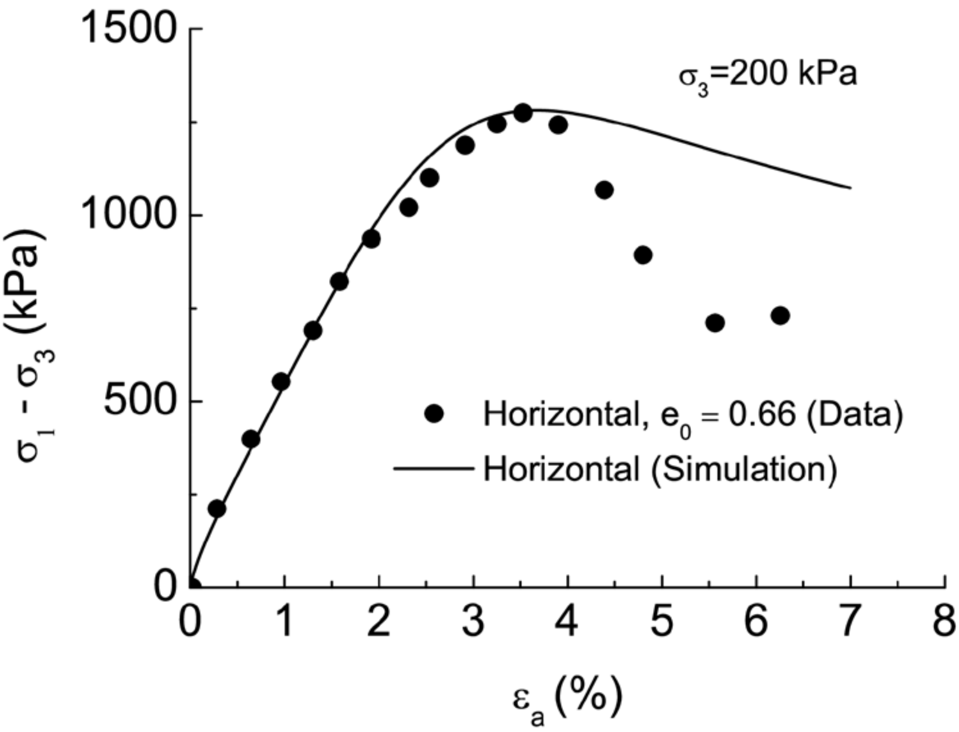

Fig. 18a

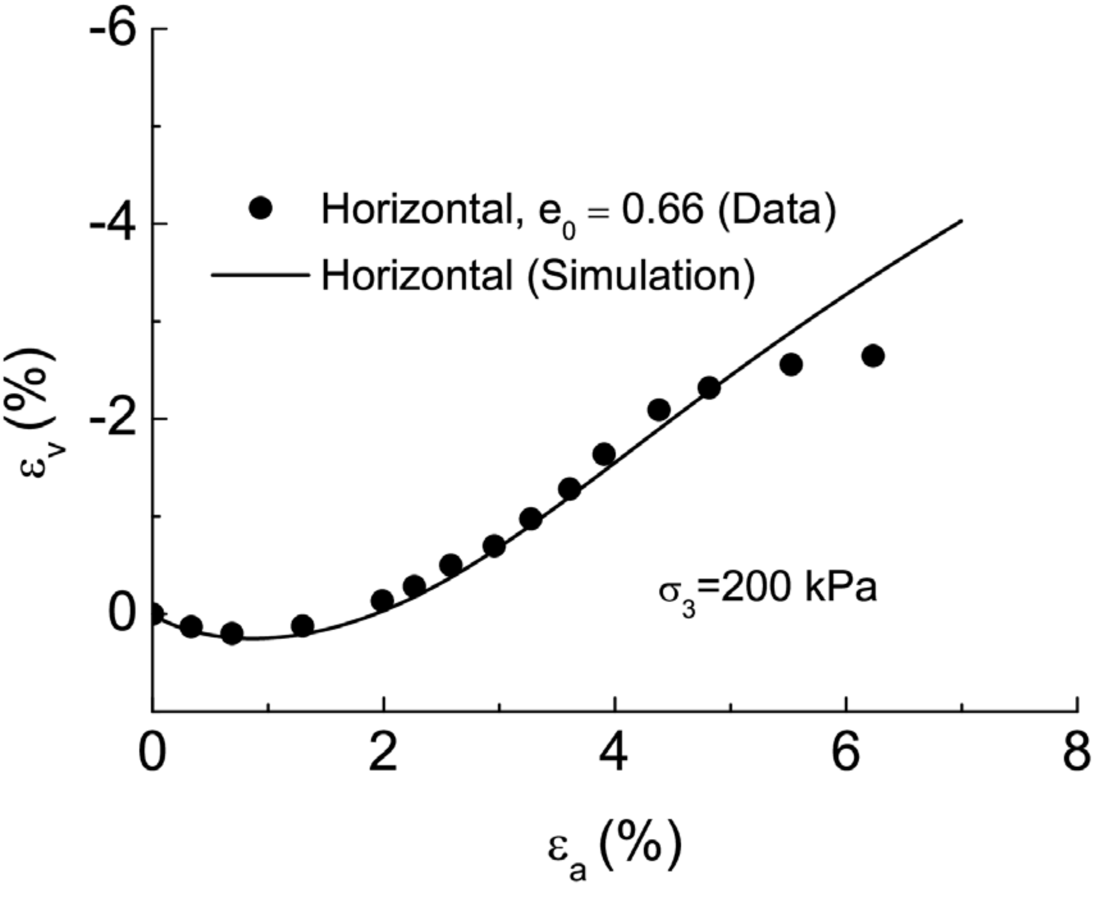

Fig. 18b

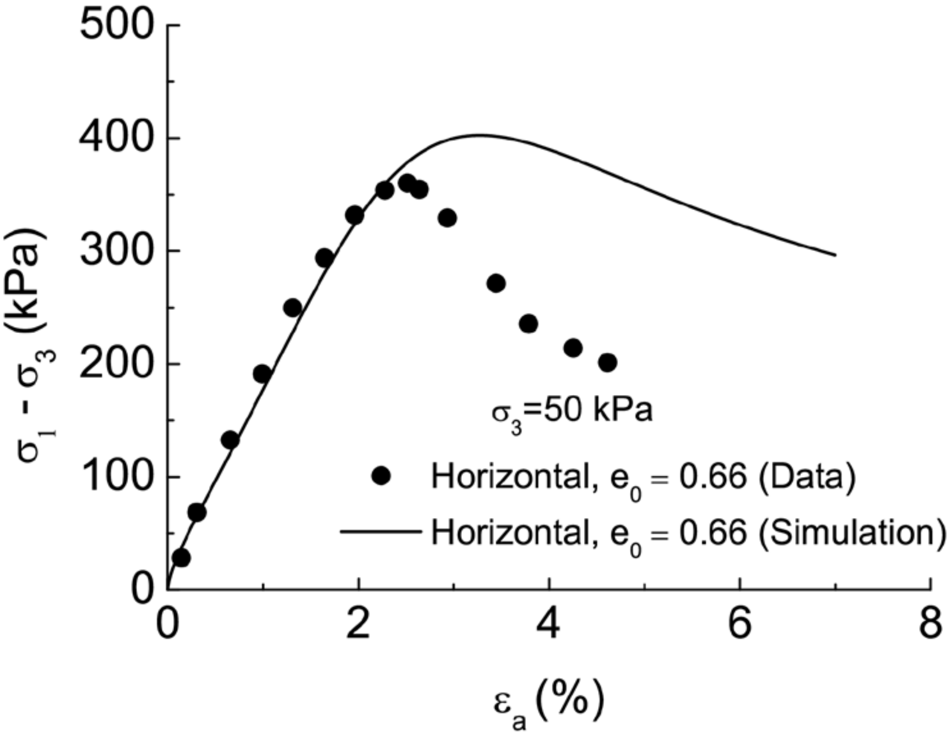

Fig. 18c

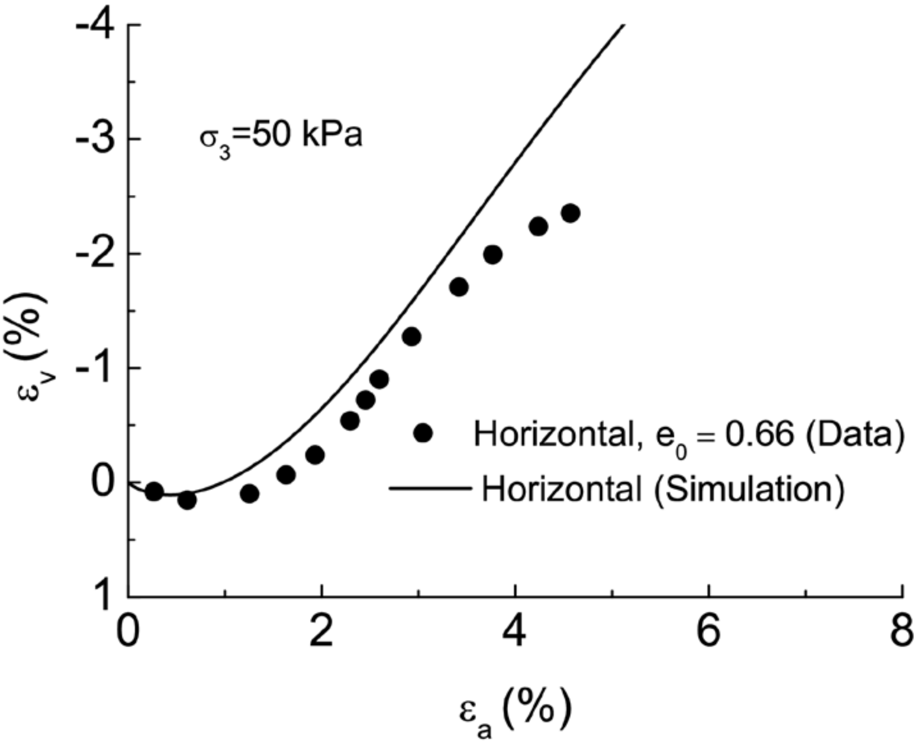

Fig. 18c

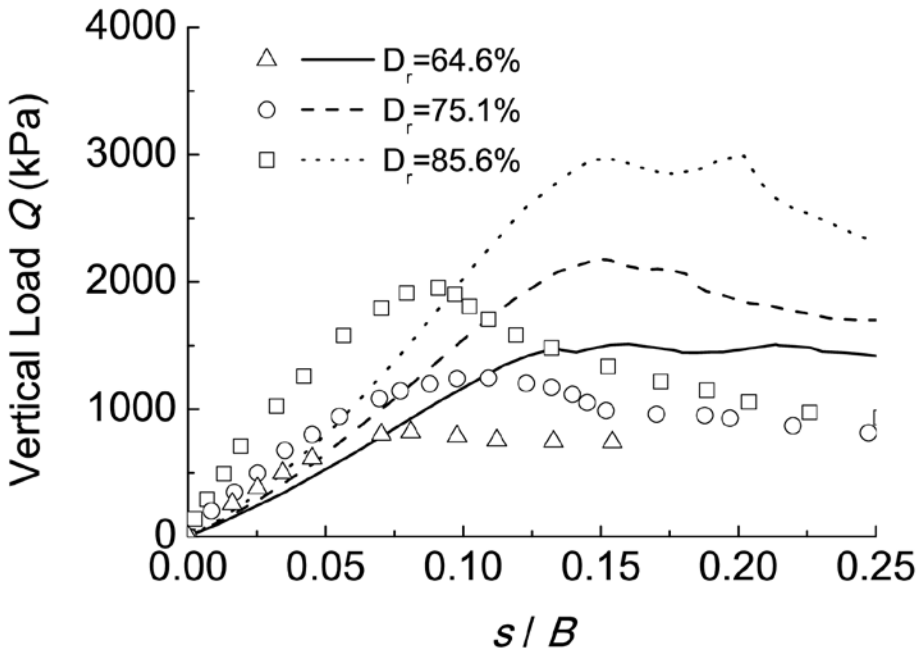

Vertical Load Q (kPa)
4000
3000
2000
1000
0
0.00
0.05
0.10
0.15
0.20
0.25
s / B
D_r=64.6%
D_r=75.1%
D_r=85.6%

Fig. 19